BG

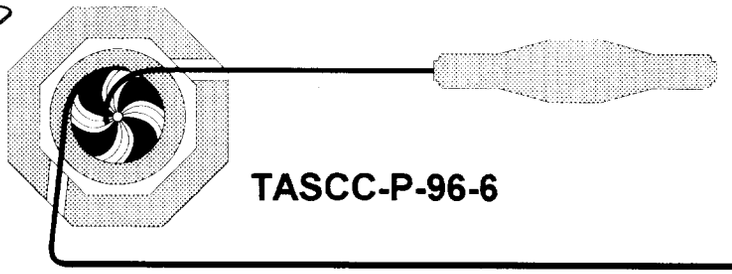

PREPRINT

TASCC-P-96-6

tascc

Lifetime Measurements of Strongly Deformed Rotational Bands in ^{133}Pm

A. Galindo-Uribarri, D. Ward, H.R. Andrews, G.C. Ball, D.C. Radford and V.P. Janzen
AECL, Chalk River Laboratories, Chalk River, Ontario, Canada K0J 1J0

S.M. Mullins[1] **and J.C. Waddington**
Department of Physics and Astronomy, McMaster University, Hamilton, Ontario, Canada *L8S 4M1*

A. Afanasjev[2] **and I. Ragnarsson**
Department of Mathematical Physics, Lund. Inst. of Technology, P.O. Box 118, S-221 00 Lund Sweden

1) Present address, Department of Nuclear Physics, Research School of Physical Sciences, Australian National University, Canberra, ACT, Australia

2) Permanent address, Nuclear Research Centre, Latvian Research Centre, Latvian Academy of Sciences, LV-2169, Salaspils, Miera str. 31, Latvia

Submitted to
Phys. Rev. C

Physical and Environmental Sciences
Chalk River Laboratories
Chalk River, ON K0J 1J0 Canada

1996 February

Abstract

We have measured lifetimes and deduced deformation parameters for rotational bands in ^{133}Pm by the DSAM. A strongly-coupled band based on the configuration with a hole in the $g_{9/2}$ orbital has deformation parameter β_2 = 0.40 (5), which is comparable to or larger than typical superdeformed bands in the A~130 region. We observe this band in ^{133}Pm down to its I=K=9/2 band head. Calculations with a configuration-dependent shell correction to the cranked Nilsson potential can explain the existence of such low-spin superdeformed structures in the A~130 region. These shapes, which also occur in ^{129,131}Pr, can be observed experimentally because of relatively low-lying shell gaps for β_2 = 0.4 near Z=58, N=72. No high-spin intruder orbitals ($\upsilon i_{13/2}$) are occupied (over the spin ranged observed); however the strongly deformation-driving properties of a hole in the extruder $\pi g_{9/2}$ orbital appear to be an essential ingredient in lowering the energy of the superdeformed shape.

PACS numbers: 21.10 Re, 23.20 Lv, 27.60 + j.

1. INTRODUCTION

There is presently a great deal of activity in the γ-ray spectroscopy of nuclei at high angular momentum. In part, this has been stimulated by the interest in superdeformed nuclei, but more generally the field is concerned with the structure of nuclei and how that structure responds to angular momentum. In this work, we focus interest on rotational bands at low excitation and angular momentum that have deformations as large as those of superdeformed bands in their mass region.

Superdeformed nuclei are generally considered to belong to the mass regions A~130, A~150, A~190 and A~240 as compiled for example by Firestone and Singh[1]. We might also consider the A~140 nuclei as separate from the A~150 region.[2] More recently, Baktash *et al.*[3] have discovered a new mass region for superdeformation near A~80.

Until recently the main ingredients for producing superdeformation were considered to be 1) large (and complementary) shell-gaps in the proton and neutron single-particle energies at the appropriate deformation and 2) the occupation of so called "intruder" orbitals. These orbitals arise from the next higher shell and intrude into the valence space because they are strongly down-sloping with increasing quadrupole deformation and rotational frequency. The significance of intruder orbitals in determining the deformation has recently been call into question by the observation of superdeformed bands in ^{129}Pr and ^{131}Pr where no intruder orbitals are occupied[4,5]. Furthermore, our recent lifetime measurements for the superdeformed bands of ^{129}Ce,[6] ^{131}Ce and

^{132}Ce[7] (Q_o = 6.1, 6.4, and 7.1 eb) respectively, suggest that the polarizing effect of neutrons in the $i_{13/2}$ orbitals is small in the Ce isotopes.

Our motivation in studying ^{133}Pm was to examine the spectroscopy, and to measure lifetimes for the $\pi g_{9/2}^{-1}$ configuration, which the earlier work in $^{129,131}Pr$ suggested could be superdeformed.

2. EXPERIMENTAL

The Tandem accelerator of the TASCC facility at AECL's Chalk River Laboratories provided a beam of ^{40}Ca ions at 176 MeV. The beam (typically 4 pna) was directed onto a target comprising a ruthenium foil of 400 $\mu g\ cm^{-2}$ enriched to 98% in ^{96}Ru, backed with a gold foil of 12.5 $mg\ cm^{-2}$. The gold foil was thick enough to stop recoils from fusion reactions. Gamma-ray spectroscopy was performed with the 8π spectrometer which comprises 20 HPGe detectors with BGO anti-Compton shields, and a spherical shell of 71 BGO scintillation detectors. Events were processed and written to tape on a trigger exceeding K hits on the BGO ball (where $K \geq 9$) and M hits on the HPGe array (after suppression) where $M \geq 2$.

A variety of replay programs were used in processing the data. For the spectroscopy of ^{133}Pm, all coincident pairs recorded in the HPGe array were stored in an $E\gamma$-$E\gamma$ coincidence matrix with conditions on the sum γ-ray energy, H, registered in the BGO ball, $12 < H < 25$ MeV. This range was chosen to enhance the 3-particle-out channels, e.g. ^{133}Pm, at the expense of the 2-particle (higher H) and four-particle (lower H) channels (cf fig. 1). This matrix contained 154 x 10^6 pairs.

For the application of DSAM techniques, events were sorted into two matrices having in case 1 an event at any HPGe detector angle versus an event in the forward ring (+37°), and in case 2, any angle versus the backward ring (-37°). The same conditions on H were applied and these matrixes contained approximately 80 x 10^6 pairs. For applications of γ - γ directional correlation techniques (afterwards called DCO ratios) a variety of matrices were constructed, but the most useful results were obtained by considering intensity ratios between a matrix containing only ± 37° pairs and a matrix containing only ±79° pairs. The same conditions on H were applied, and these matrices contained approximately 43 x 10^6 and 31 x 10^6 pairs respectively.

3. ANALYSIS

3.1 Level scheme:

The level scheme for ^{133}Pm has been studied most recently by Regan *et al.*[8] The present level scheme is shown in Figure 2 where we have used their nomenclature for labelling the bands. Our results are in general agreement as regards bands 1-4; in addition, we see transitions linking band 3 to band 1, which allow us to fix their relative excitation energies as well as that for band 4. As shown later, these linking transitions are $\Delta J = 0$ and fix the spins of bands 3 and 4 to be one unit lower than assigned in reference 8. We also found a new band (band 7) that decays to bands 1/2 over the spin range 15/2 - 31/2.

The main area of disagreement concerns how bands 5 and 6 are attached to the level scheme. Our scheme is based on γ-γ coincidence spectra of the quality illustrated in Figure 3. We suggest that the corresponding spectrum shown in Reference 8 (Figure 9) contained impurity

transitions in the gates which show γ410 and γ263 keV of band 2. These two γ-rays are not in coincidence with bands 5 and 6 in our data (cf Figure 3).

The linking of bands 5 and 6 to bands 3 and 4 in our scheme indicates a much lower spin-value for the bandhead than was suggested in Reference 8, and as shown below, we propose that these bands are superdeformed and are based on configurations containing a hole in the $\pi g_{9/2}$ orbital, i.e. a $[404]_{9/2}$ Nilsson assignment. They therefore belong to the same configuration as the superdeformed bands found in ^{129}Pr[5] and ^{131}Pr[4].

3.2 Directional Correlations (DCO Ratios)

Gamma-ray transition energies, intensities, DCO ratios, and assignments are given in Table 1. A DCO Ratio is defined from the intensity of a given pair of coincident transitions in the two matrices corresponding to ±37°/±37° and ±79°/±79° correlations:

$$DCO = I\gamma\gamma^{\text{coinc pair}}\ (\pm 37^{\circ},\pm 37^{\circ})/I\gamma\gamma^{\text{coinc pair}}\ (\pm 79^{\circ}/\pm 79^{\circ}) \qquad (1)$$

The gamma-ray intensities must be corrected for detection efficiency. If the coincident pair are known to be stretched E2 transitions, then the DCO ratio provides a measure of the nuclear spin alignment.

In this work, calculated DCO ratios take an initial state of high spin with a particular degree of spin alignment parameterized by a gaussian distribution of m- substates centred at m = 0, and the

standard deviation, σ, is expressed as a dimensionless factor, σ/J. This initial state is assumed to decay by unobserved stretched transitions to the state of interest, which defines σ/J (in the calculation) for subsequent states.

DCO ratios were calculated for all common γ_1 - γ_2 correlations as a function of σ/J, J, and the mixing ratio δ = E2/M1 where applicable. These calculations are specific to our geometry $\theta_1 = \pm 37^\circ$, $\theta_2 = \pm 79^\circ$ and results are averaged over the azimuthal variables appropriate to the instrument.

The spin-alignment given by the DCO ratios (cf Table 1) for strong pairs of transitions both of which have stretched E2 character (DCO =1.99 ± 0.06) corresponds with $\sigma/J = 0.23 \pm .03$ at J = 17.

A powerful method to extract E2/M1 mixing ratios (δ) for transitions between signature-degenerate bands is to choose neighbouring J→(J-1) transitions as the coincident γ-γ pair in a DCO ratio. In general, such a DCO ratio cannot be interpreted since two unknown mixing parameters δ_1 and δ_2 enter into it. However, in signature-degenerate bands, the mixing ratio must change very slowly with spin, except at a sharp alignment gain. We have exploited this property by evaluating DCO ratios for J→(J-1) → (J-2) γ-γ pairs where δ is in common.

3.3 Spin Assignments:

Band 3: The three transitions linking band 3 to band 1 must change parity since the parities of

these bands are established[8]. Furthermore, we may assume that any M2 mixing would be extremely weak, since these transitions compete with collective E2's in band 3. Therefore, the DCO-values shown in Table 1 are compatible only with J→J assignments (DCO = 1.93 for δ = 0) and not with J→J±1 (DCO = 1.13 for δ = 0).

Band 7: Band 7 decays to band 1 and band 2 over a spin range 15/2 - 31/2 and with any plausible choice for the spins, it follows that either the set of transitions to band 1 or the set to band 2 must have J→J±1 assignments. Table 1 shows that both these sets have DCO ratios near the value DCO = 2, and therefore, the set with J→J±1 assignment must have strongly mixed E2/M1 character which implies negative parity for band 7. The DCO ratios do not allow us to distinguish which sequence has J→J±1 and we chose the most plausible assignment.

Band 5/6: The observed branching and DCO ratios restrict the band head (654 keV) to spin 5/2, 7/2 or 9/2. Our assignment of 9/2 is based on the fact that the bands are signature-degenerate partners of a high-K, 1-quasiparticle orbital for which the only candidate acceptable to theory is the $\pi g_{9/2}$. As shown later, analysis of B(E2) ratios in these bands shows that the K-value is 9/2, and the measured B(M1)/B(E2) ratios are consistent only with $\pi g_{9/2}$.

The state at 372 keV is most probably $7/2^+$.

3.4 Analysis of B(M1) and B(E2) Values Between Signature-Partner Bands:

Table 2 shows results for the branching ratios, and E2/M1 mixing ratios (δ) measured for

transitions between the signature-partner bands 3/4, 5/6 and 1/2. For the case of bands 3/4 we have compared results for the mixing ratio derived from DCO-values involving mixed-E2, with those derived from mixed-mixed sequences. The agreement is seen to be good, with the mixed-mixed analysis giving a more precise value. This is because the gradient of the function DCO versus δ in the mixed-mixed case is approximately double that in the conventional analysis (mixed-E2). For band 5/6, the advantage of this method is even greater since the E2 transitions are very weak.

From the branching ratios and mixing ratios we have evaluated the ratios B(M1;J→J-1)/B(E2; J→J-2) and B(E2; J→J-1)/B(E2; J→J-2) shown in Table 2 and in Figures 4 and 5. The B(E2) ratios are very sensitive measures of the K-value for the band. Clearly in Figure 5, bands 5/6 have K = 9/2 and bands 3/4 have K = 3/2 character.

The B(M1)/B(E2) ratios for signature-degenerate bands with no spin alignment are sensitive measures of the configuration through the g-factor, g_K, and the K-value. Spin-alignment is a complicating factor, but it can be taken into account with the geometric model of Donau and Frauendorf[9]: we have for a 3-quasiparticle state:

$$B(M1: J \rightarrow J-1) = \tfrac{3}{8\pi} K^2/J^2 \{ (g_K - g_R) [(J^2 - K^2)^{1/2} - i - (g^{(2)} - g_R) i^{(2)} \}^2 \mu_N \qquad (2)$$

where g_R is the g-factor for collective rotation and i is the aligned spin of the 1-quasiparticle orbit

that contributes both its signatures to the band. The 2-quasiparticle component has alignment $i^{(2)}$ and g-factor $g^{(2)}$.

Assuming $g_R = Z/A = 0.46$, and our measured Q_o-values (see section 3.5), we compare the measured B(M1)/B(E2) ratios with those calculated from eq. 2 with $g_K(\pi g_{9/2}) = 1.27$, $g_K(\pi h_{11/2}) = 1.17$, $g_K(\pi d_{5/2}) = 1.38$ and $g_K(\pi g_{7/2}) = 0.72$, which are standard values for the region originally suggested by Lonroth *et al.*[10]. The 1-quasiparticle alignments were taken from experiment: i = 0,1 and 4 for bands 5/6, 3/4 and 1/2 respectively. Bands 3/4 and 1/2 experience an alignment gain, $i^{(2)}$, which was taken from experiment and assumed to arise from the $\pi(h_{11/2})^2$ configuration.

The results are shown in Figure 4. We find good agreement with the ($g_{9/2}$, K = 9/2) assignment for bands 5/6. For bands 3/4, the best agreement is obtained for a $\pi d_{5/2}$, K = 3/2 configuration, however with the experimental aligned spin included as in eq. 2, the calculation is about a factor of two too small. Nevertheless, the only other plausible assignment, $\pi g_{7/2}$, K = 5/2 is ruled out by the experimental determination of the K-value = 3/2 (see fig. 5) and by the calculated B(M1)/B(E2) ratios for a $\pi g_{7/2}$, K = 5/2 configuration, which are an order of magnitude smaller than the observed values for bands 3/4. This is readily understood from the Schmidt rules which give a much larger magnetic moment for $\pi d_{5/2}$ than for $\pi g_{7/2}$.

The transitions from band 2 to band 1 have very small B(M1) values as seen in Figure 4. This is consistent with the geometric model and indicates a near cancellation of the term $(J^2-K^2)^{1/2}$

with the aligned spin term, i, at low spin in eq. 2. The sign of the mixing ratio, δ, was measured to be positive (cf Table 2) therefore, the term $(J^2-K^2)^{1/2} > i$ for $J \geq 13/2$. A rise in the experimental B(M1) with spin is expected from eq. 2, but the detailed shape is not reproduced in Figure 4.

3.5 DSAM Analysis:

We have made a DSAM analysis of bands 1-6 in ^{133}Pm. Because bands 5 and 6 are strongly coupled, and show nearly degenerate signature partners with strong connecting dipole transitions, they had to be analyzed as a pair. Bands 1-4 could be analyzed as individual bands; although they have significant branching at low spin, this becomes negligible for spins above 31/2 where the DSAM analysis was performed. Typical spectra are shown in Figures 6 and 7. The DSAM code used as input the electronic stopping powers in tabular form and we took scaled[11] Northcliffe and Schilling values[12]. The nuclear stopping was treated according to the formulae of Lindhard *et al.*[13] as parameterized by Winterbon[14]. Corrections for multiple scattering were introduced according to the prescription of Blaugrund[15]. The code analyzed peak centroids or full lineshapes for either a single band or for signature-partner bands, in which case branching ratios were entered as input. The time history for feeding the band was simulated by adding extra transitions at the top of the cascade, and by introducing side feeding at each stage of the cascade. The side feeding was parameterized as a rotational band with an intrinsic quadrupole moment, Q_o(SF), and moment of inertia, of $I^{(1)}$(SF); the sidefeeding intensities were taken from experiment.

Centroid shifts extracted from the data and normalized to the maximum possible shifts (F-values) are shown in Figure 8. The simplest analysis is to assume that the lifetimes in the band are given by a rotational model, and that the time history of side feeding is the same as that for feeding down the band. We have:

$$T(E2) = 1.225 \times 10^{13}\, E_\gamma^5 . B(E2) \qquad \text{sec}^{-1} \qquad (3)$$

$$B(E2;\, J_i \rightarrow J_f) = 5/16\pi\, Q_o^2 \langle J_i\, K\, 2\, 0 | J_f\, K \rangle^2 \qquad e^2b^2 \qquad (4)$$

where E_γ is in MeV, and the B(E2) in units of e^2b^2. We can then fit the F-curve with only one free parameter, namely Q_o. At the next level of sophistication one can assume that the sidefeeding has a systematic character and can be parameterized with Q_o(SF). There are then two free parameters to fit the F-curve. In the case of large side feeding intensity, there will be a large covariance between the parameters Q_o and Q_o (SF) which limits the accuracy on Q_o. To some degree, this uncertainty can be reduced by appealing to the lineshapes which have a sensitivity to Q_o (SF) beyond that expressed in the centroids. It was not straightforward to assign uncertainties in the analysis. We have considered fits allowing Q_o to vary with spin. Although there is some indication that Q_o increases with decreasing spin, these effects are not outside the uncertainties. The adopted values and uncertainties quoted in Table 3 represent averages of different analyses with an uncertainly large enough to encompass the spread of the results.

Band 1: The processed spectra were from a single gate set on γ 675 keV (Figure 6). The F-curve is shown in Figure 8. Because the side feeding was very strong, there was a large

covariance between Q_o (band) and Q_o (SF), resulting in a flat minimum of χ^2 extending from approximately Q_o (band) = 5, Q_o (SF) = 5, to Q_o (band) = 7.5 Q_o (SF) =2. The lineshape analysis ruled out the extremes of slow and fast sidefeeding discussed below and agrees best for a sidefeeding history identical to that coming down the band. Results are summarized in Table 3.

Bands 3/4: The spectra processed were sums of coincidence gates set on $E\gamma$ = 168, 421, 536 and 567 keV for band 4 and gates set on $E\gamma$ = 130, 358 and 510 keV for band 3. The data were similar to band 1 and are not shown. The sidefeeding was less severe than for band 1, and definitive results could be obtained by allowing Q_o (band) and Q_o (SF) to vary freely.

Bands 5/6: The F-curve (figure 8) was generated from spectra obtained with a single gate on γ181 keV; for higher statistical accuracy at the expense of bringing in contaminating transitions, the lineshapes, figure 7, were analysed from a sum of gates set on low spin transitions. There was relatively little side-feeding into these bands, but there was a problem in defining the feeding history at high spins, since the fastest observed transitions had F $\cong$ 0.5 (of Figure 7). In this case we simulated the history at high spin by extending the level scheme by four rotational cascades in each signature above the highest spins observed. The branching ratios between signatures were extrapolated with the parameters shown in Figure 4. The Q_o for these extrapolated cascades was allowed to vary freely with Q_o (band). The sidefeeding was assumed to have the same history as that feeding down the bands.

Lineshape analysis is shown in Figure 7. The fit to the transitions at 704 and 660 keV is improved by increasing Q_o band as indicated in Figure 7.

4. COMPARISON WITH THEORY AND DISCUSSION

The measured deformation of bands 5/6 (β_2 = 0.40) is comparable to that of the most superdeformed rotational band in the region[7] (namely ^{132}Ce which has β_2 = 0.39). In Figure 9(a) we compare dynamical moments of inertia for some known superdeformed bands in nuclei with $72 \leq N \leq 74$. The signature- partner bands shown in ^{133}Pr were assigned by Wilson *et al.*[16] to the high spin configuration with a proton hole in the $g_{9/2}$ orbital. The comparison in Figure 9 suggests to us that typical high-spin superdeformed bands i.e. ^{132}Ce, ^{133}Pr and ^{133}Nd differ from the low-spin bands i.e. ^{129,131}Pr and ^{133}Pm in that they contain additional aligned components presumably $\pi h_{11/2}$, $\upsilon h_{11/2}$ and/or $\upsilon i_{13/2}$. These contribute to the dynamical moment of inertia, but do not change the deformation very much. To see this more explicitly we have compared the aligned spin in the yrast superdeformed bands of ^{133,135,137}Nd referenced to the superdeformed bands in ^{133}Pm in figure 9(b). These Nd isotopes are the only high-spin superdeformed bands in the A~130 region for which firm spin assignments are known[17]. The analysis demonstrates that there is a relatively constant (with rotational frequency) alignment gain of approximately $5\hbar$ between the high-spin superdeformed bands and the ^{133}Pm bands. In our interpretation there will be high-spin superdeformed bands in ^{131}Pr and ^{133}Pm with aligned particles coupled to $\pi g_{9/2}^{-1}$: conversely, we would expect that the pure $\pi g_{9/2}^{-1}$ structure should occur at low excitation in ^{133}Pr. We note that there need be no strong or even measurable decay path between the $\pi g_{9/2}^{-1}$ and $\pi g_{9/2}^{-1} \otimes$(aligned particle) structures: this follows because these bands lie well above yrast, and

therefore at the critical frequency for de-alignment, the decay path will mainly go to the yrast line, rather than following through a backbending pattern.

To understand the reasons for the co-existing deformations at low spin in ^{133}Pm we have performed calculations within the configuration-dependent shell correction approach using the cranked Nilsson potential[18]. The (K, μ) parameter set from ref. 18 was used in the present calculations for the parameterization of the Nilsson potential. These calculations suggest that the superdeformed band has the configuration $\pi(g_{9/2})^{-1}\ 5^6 \otimes \upsilon\ (h_{9/2},\ f_{7/2})^2\ 5^8$, where 5^6 denotes the high-j particle configuration $(h_{11/2})^6$. It should be noted that the labelling is only approximate and that the full Nilsson Hamiltonian was diagonalizaed in the calculations. Compared to the normal deformed configuration, the superdeformed core has two neutrons in $[541]_{1/2}$ (originating in the $h_{9/2}$, $f_{7/2}$ subshells); two protons in $[532]_{5/2}$ (originating in the $h_{11/2}$ subshell); and a proton hole in $[404]_{9/2}$ (originating in the $g_{9/2}$ subshell). These shell-gaps are readily seen in the single-particle energies of a Woods-Saxon or Modified oscillator potential (for example ref. 4); the normal core for Z=60 N=72 is centred near β_2 ~0.25 - 0.30 whereas the "excited" Z=60 N=72 core is centred near β_2 ~ 0.4 - 0.45. In our calculations, the energy needed to excite to the higher core (with $\pi(g_{9/2})^{-1}$) is only 640 keV.

The predicted configurations relative to an arbitrary rigid rotor reference are shown in Figure 10 and Figure 11. The lowest configuration $\pi 5^4 \upsilon 5^8$ is predicted to have the odd proton in $(d_{5/2}/g_{7/2})$ in agreement with experiment. The calculated deformation is $\varepsilon_2 = 0.261$, $\varepsilon_4 = 0.021$, $\gamma \sim 0^\circ$ for the states with $I = 3^+/2$ and $I = 5^+/2$ (band-heads of bands 3 and 4). Assuming a uniform charge

distribution and that the matter distribution coincides with the charge distribution, we can estimate the charge quadrupole moment Q_o from the expression (Ref. 19):-

$$Q_o = \frac{4}{5} Z r_0^2 A^{2/3} [\varepsilon_2 (1 + \frac{1}{2}\varepsilon_2) + \frac{25}{33}\varepsilon_4^2 - \varepsilon_2\varepsilon_4] \frac{\cos(\gamma + 30°)}{\cos(30°)} \qquad (5)$$

Assuming r_o = 1.2 fm, this gives Q_o = 5.3 eb for states with I = $3^+/2$ and I = $5^+/2$, which is in good agreement with the experimental value (cf Table 3). The superdeformed band head $[g_{9/2}]^{-1}$ is predicted to lie ~640 keV above yrast and has a calculated deformation ε_2 = 0.363, ε_4 = 0.036, $\gamma = 0^o$ at I = 9/2 corresponding to Q_o = 7.57 eb. In the experiment, the band head lies 272 keV above yrast and Q_o = 7.4 ±1.0 eb (of Table 3).

The calculation reproduces the near signature-degeneracy of the superdeformed $(g_{9/2})^{-1}$ and the $d_{5/2}$ configurations as shown in Figures 11 and 12. With increasing spin, the excitation energy of the superdeformed band relative to the $d_{5/2}$ band increases both in the experiment and in the theory (see Figures 11 and 12). However, the calculations overestimate the excitation energy of the superdeformed band. For example, at $I = \frac{41}{2}$, $E_{SD} - E_{d_{5/2}} = 1.367 MeV$ in the calculation versus 0.535 MeV in the experiment.

In these calculations, the structure of the typical high-spin superdeformed band in ^{133}Pm is predicted to be $\pi 5^4 6^1\ \upsilon 5^6[h_{9/2}\ f_{7/2}]6^2$ for positive signature (cf.Figure 10), and $\pi 5^4\ \upsilon 5^6[h_{9/2}\ f_{7/2}]^2\ 6^2$ for negative signature (cf.Figure 11). Relative to the low-spin strongly-coupled superdeformed

band, these bands contain two neutrons in the intruder $i_{13/2}$ (N=6) orbital and either zero or one proton in the intruder $i_{13/2}$ (N=6) orbital. They are predicted to become yrast at around spin 45$\hbar$. However, despite the intruder content, their deformation is predicted to be smaller than that for the low-spin superdeformed band (cf.Figures 10 and 11 and Table 4). This is partly due to the fact that the bands are considered at different spin values; namely for the fixed configurations considered here, there is a general tendency that the deformation decreases with spin, as can be seen in table 4. One should also note that the shape polarization from $g_{9/2}$ holes appears comparable or even larger than from high-j $\upsilon i_{13/2}$ particles. In the present experiment we would not expect to see high-spin superdeformed bands since firstly the angular momentum input, I_{max} ~44$\hbar$, is close to the predicted yrast crossing spin, and secondly, the backed target would have introduced Doppler smearing.

It is worth examining whether the observed band crossings are consistent with the measured deformations. From the experimental routhians shown in fig. 13, the $\pi(h_{11/2})^2$ crossing occurs in bands 3/4 at $\hbar\omega$ = 0.27 MeV, whereas in a cranked shell-model (CSM) with standard parameters, at β_2 = 0.29 (as measured), the crossing frequency is predicted to be $\hbar\omega$ = 0.30 MeV: the observed crossing frequency corresponds with β_2 = 0.275. (Figures illustrating these remarks may be found in ref. 8).

The first pair of protons to align from $\pi(h_{11/2})^2$, the AB crossing in CSM terms, is blocked in bands 1/2 and the second $\pi(h_{11/2})^2$ pair (BC) are predicted to cross at $\hbar\omega$ = 0.46 MeV, for the measured deformation β_2 = 0.29, versus an observed crossing frequency at $\hbar\omega$ = 0.39 MeV

(fig. 13). Conversely, the observed crossing frequency corresponds with $\beta_2 = 0.25$.

For the above-mentioned bands, this level of agreement is perhaps as good as could be expected since systematically the $\pi(h_{11/2})^2$ crossings are lower than predicted with a standard CSM in odd-Z nuclei. This is because the odd proton will partially quench the proton pairing field, making it easier to align protons. Despite the fact that the $\pi(h_{11/2})^2$ AB alignment is open, the superdeformed bands 5/6, assigned $\pi g^{-1}_{9/2}$, show no crossings up to the highest frequency observed $\hbar\omega$ ~0.46 MeV (fig. 9b). The predicted crossing frequency is a strong function of deformation, and from the CSM results we note that the non-appearance of this crossing by $\hbar\omega$ ~0.46 MeV implies a deformation $\beta_2 > 0.41$. This is consistent with our measured deformation. The $\upsilon(h_{11/2})^2$ has the opposite dependence on deformation to the $\pi(h_{11/2})^2$ alignment i.e., it moves to lower frequency with increasing deformation. For the superdeformed bands 5/6 at the measured deformation ($\beta_2 = 0.40$) the predicted crossing frequency is $\hbar\omega = 0.46$ MeV. Its non-appearance is also consistent with our measured deformation. The CSM therefore predicts that for $\beta_2 = 0.4$, the $\upsilon(h_{11/2})^2$ and $\pi(h_{11/2})^2$ alignments will occur simultaneously at $\hbar\omega$ ~0.46 MeV. This is just the frequency where we lose sight of the band in the experiment, and it suggests that a large alignment gain and structural change are the underlying cause.

Several years ago, Leander and Möller[20] made a theoretical study of groundstate deformations at the boundary between the near-spherical light rare-earth region near N=82, and the then unexplored deformed region centred near N=66. An interesting aspect of that study was the prediction of a promontory of strong deformation for Pm isotopes which juts in towards the

valley of stability. In addition, a sharp transition was obtained for Pm isotopes, where the deformation was predicted to change from $\beta_2 = 0.22$ at ^{136}Pm to $\beta_2 = 0.34$ at ^{135}Pm.

Our total routhian surface (TRS) calculations with standard parameters[21] also give a sharp transition in Pm isotopes, but it occurs between ^{135}Pm ($\beta_2 = 0.23$) and ^{133}Pm ($\beta_2 = 0.31$) for (π, α) = (-, -1/2) at rotational frequency $\hbar\omega = 0.05$ MeV as shown in Figure 14. Results for other (π, α) configurations are similar. Measurements by Mullins *et al.*[22] and by Wadsworth *et al.*[23] with a recoil distance technique for ^{137}Pm ($\beta_2 = 0.201 \pm 0.009$) ^{135}Pm ($\beta_2 = 0.226 \pm 0.006$) and ^{133}Pm ($\beta_2 = 0.303 \pm 0.013$), are in very close agreement with the TRS calculations, and in good agreement with the present ^{133}Pm measurement ($\beta_2 = 0.29 \pm 0.3$), for bands 3/4.

5. CONCLUSIONS

We have measured lifetimes for several rotational bands in ^{133}Pm with the DSAM. The strongly-coupled structure based on a hole in the Nilsson proton [404] 9/2 orbital was found to have a deformation parameter $\beta_2 = 0.40 \pm 0.05$, which is as large as that of the most superdeformed band found in the A = 130 region. Its systematics follow the pattern established for ^{129,131}Pr, although the deformation in ^{133}Pm is higher. In all three cases, the band can be followed up to $\hbar\omega$ ~0.45 MeV, and it seems plausible that we lose sight of the band at the critical frequency for alignment of $\pi h_{11/2}$ and $\upsilon h_{11/2}$ quasiparticles which for the ^{133}Pm case are predicted to occur at $\hbar\omega$ ~0.45 MeV for a deformation $\beta_2 = 0.40$.

Other rotational bands in ^{133}Pm were found to have substantial deformation (β_2 ~0.29) and this

is supported both by standard TRS calculations and by the configuration-dependent shell correction approach, thus confirming the long-standing prediction of Leander and Möller that the Pm isotopes would be the most accessible (i.e. closest to β-stability) of nuclei in the deformed region centred near N = Z = 66.

It will now be of interest to search for further examples of superdeformation where the nucleus exploits shell gaps of high deformation at low spin. The next candidates might involve the shell gap at N=80, however, preliminary calculations indicate the superdeformed band-head rises rapidly in excitation, making it hard to populate and detect. Nevertheless, the sensitivity of the new generation of γ-ray spectrometers may be sufficient.

REFERENCES

[1] R.B. Firestone and B. Singh, Table of Superdeformed Nuclear Bands and Fission Isomers, 1994.

[2] S.M. Mullins *et al.*, "Proceedings of the Conference on Physics From Large γ-ray Detector Arrays", Berkeley 1994, LBL 35687., p. 24.

[3] C. Baktash *et al.*, Phys. Rev. Lett. 74 (1995) 1946.

[4] A. Galindo-Uribarri *et al.*, Phys. Rev. C 50 (1994) R2655.

[5] A. Galindo-Uribarri, D. Ward, V.P. Janzen, D.C. Radford, S.M. Mullins and S. Flibotte, AECL-11132, PR-TASCC-09 (1994) p. 3.1.15.

[6] A. Galindo-Uribarri, D. Ward, V.P. Janzen, D.C. Radford, S.M. Mullins and S. Flibotte, AECL-11132, PR-TASCC-09 (1994) p. 3.1.16.

[7] D. Ward *et al.*, "Proceedings of the Conference on Physics From Large γ-ray Detector Arrays", Berkeley 1994, LBL-35687, p. 4.

[8] P.H. Regan *et al.*, Nucl. Phys. A533 (1991) 476.

[9] F. Donau and S. Frauendorf in "High Angular Momentum Properties of Nuclei", ed. N.R. Johnson (Hardwood, New York 1982) p. 143.

[10] T. Lonnroth, S. Vajda, O.C. Kistner and M.H. Rafoilovich, Z Phys. A317 (1984) 215.

[11] S.H. Sie, D. Ward, J.S. Geiger, R.L. Graham and H.R. Andrews, Nucl. Phys. A291 (1977) 443.

[12] L.C. Northcliffe and R.F. Schilling, Nucl. Data Tables A7 (1970) 233.

[13] J. Lindhard, M. Scharff and H.E. Schiott, Mat. Fys. Medd. Dan. Vid. Selk. 33 No. 14 1963.

[14] K.B. Winterbon, Atomic Energy of Canada Limited Report AECL-3194 (1968).

[15] A.E. Blaugrund, Nucl. Phys. 88 (1966) 173.

[16] J.N. Wilson *et al.*, Phys. Rev. Lett. 74 (1995) 1950.

[17] S. Lunardi, R. Venturelli, D. Bazzacco, C. Rossi-Alvarez, C.M. Petrache, G. de Angelis, D. Bucurescu and C. Ur., Proceedings of the "Conference on Physics from Large γ-ray Detector Arrays", Berkeley 1995 LBL 35687 Vol. 2, p. 247.

[18] T. Bengtsson and I. Ragnarsson, Nucl. Phys. A436 (1985) 14.

[19] W. Nazarewicz and I. Ragnarsson, Nuclear deformations, in Handbook of nuclear properties, eds. D.N. Poenaru and W. Greiner (Oxford Press, Oxford, to be published).

[20] G.A. Leander and P. Möller, Phys. Lett. 110B (1982) 17.

[21] W. Nazarewicz, R. Wyss and A. Johnson, Nucl. Phys. A503 (1984) 285.

[22] S.M. Mullins, M.D. Cohler, A. Ghazarian, J.R. Hughes, R. Wadsworth, D.L. Watson, P.J. Bishop, A.J. Kirwan, P.J. Nolan, R.J. Poynter and J. Heese, J. Phys. G: Nucl. Phys. 14 (1988) 1373.

[23] R. Wadsworth, J.M. O'Donnell, D.L. Watson, P.S. Nolan, P.S. Bishop, D.J. Thornley, A. Kirwan and D.J.G. Love, J. Phys. G 13 (1987) 205.

FIGURE CAPTIONS

Figure 1 Projections of the γ-γ coincidence matrix. Good separations of channels involving 2 (top panel), 3 (bottom panel) and 4 particles out was obtained by gating on the total energy parameter H recorded in the BGO ball. Only transitions of special interest are labelled. Transitions without a nucleus assignment are assigned to ^{133}Pm. Approximately 275 transitions were placed in the level schemes of ^{133}Pm, ^{133}Sm, ^{130}Nd, ^{132}Nd and ^{134}Sm. Transitions marked with * and ** are members of long cascades with irregular spacings that are assigned to ^{99}Pd and ^{96}Ru arising from reactions with ^{63,65}Cu which contaminated the target during the electrodeposition process.

Figure 2 Level scheme for ^{133}Pm from this work. Note that the lowest state shown need not be the ground state, since this experiment was not sensitive to isomeric decays.

Figure 3 Coincidence spectrum with γ181 keV (labelled in Figure 1) showing the strongly-coupled superdeformed band in ^{133}Pm and its linking transitions (*) to the normal states (*.*). Note that the vertical scale cuts-off the peaks at 157 and 205 keV.

Figure 4 Measured and calculated B(M1)/B(E2) ratios for transitions between signature partner bands in ^{133}Pm. The solid line for Band 5/6 and the dashed line for Band 3/4 were calculated with no spin alignment. The solid lines for Bands 3/4 and 1/2 use the experimental spin

alignment with the Donau-Frauendorf formalism (cf.text).

Figure 5 Calculated (solid line) and measured ratios of B(E2) - values between signature partner bands. In a rigid rotor model these are given as the ratio of the appropriate Clebsh-Gordon coefficients (solid lines) which have a strong dependence on the K-quantum number.

Figure 6 Top panels: spectra in coincidence with γ675 keV in Band 1, selected on all angles and projected for detectors in the +37° and -37° rings.

Bottom panels: background subtracted Doppler-broadened lineshapes derived from the spectra shown in the top panels and compared with a lineshape calculation (cf.text). The fit shown corresponds with Q_o=5.0 eb ($J \geq 43/2^-$ $E\gamma \geq 934$ keV); Q_o = 5.2 eb ($J = 39/2^-$ $E\gamma$ = 866 keV); Q_o = 5.6 eb ($J = 35/2^-$ $E\gamma$ = 804 keV) and Q_o=5.8 eb ($J=31/2^-$ $E\gamma$ = 747 keV).

Figure 7 Top panels: Spectra in coincidence with low-spin transitions in Band 5/6 selected on all angles and projected for detectors in the +37° and -37° rings.

Bottom panel: background-subtracted Doppler broadened lineshapes from the spectra shown in the top panels compared with a lineshape calculation (cf text). The fits shown correspond to Q_o = 7.35 eb for $J > 29/2$, $E\gamma > 704$ keV and Q_o= 8.3 eb for $J \leq 29/2$, $E\gamma \leq 704$ keV.

Figure 8 Experimental and fitted values of the ratio F = (observed centroid shift/maximum shift) for rotational bands in ^{133}Pm. The fits shown for Band 1 corresponds to Q_o = 5.0 eb ($J \geq 43/2^-$ $E\gamma \geq 934$ keV) Q_o = 5.2 eb ($J = 39/2$ $E\gamma$ = 866 keV) and Q_o = 5.6 ($J \leq 35/2$ $E\gamma \leq 804$ keV).

The figure shown for Band 5/6 corresponds with Q_o = 7.35 eb. The staggering in the fitted value is an artifact of including a finite number of precursor transitions (cf text) so that the two signatures do not see exactly the same delay in the feeding process.

Figure 9(a) Typical dynamical moments of inertia $I^{(2)}$ for bands believed to have superdeformed character in the A~130 region. To keep the figure as clear as possible, not all band members are shown in all nuclei.

Figure 9(b) Aligned spins in ^{133,135,137}Nd yrast superdeformed bands relative to the superdeformed bands (5/6) in ^{133}Pm. These Nd isotopes were chosen because they are the only high spin superdeformed bands in the A~130 region with firm spin assignments.

Figure 10 Calculated low-lying configurations of positive parity and signature α=+1/2 in ^{133}Pm relative to a rigid rotor reference. The configurations are labelled by the number of particles in the high-*j* orbitals of the N=5 ($h_{11/2}$) and N=6 ($i_{13/2}$) shells and by the number of particles in the $h_{9/2}/f_{7/2}$ subshells as well as the number of holes in the $g_{9/2}$ subshell. The deformations given for specific configurations correspond to spins where they are yrast. The normal-deformed yrast configuration is $\pi 5^4.\upsilon 5^8$ or $\pi d_{5/2}$ (Bands 3/4 in the experiment). The superdeformed configuration is $\pi[g_{9/2}]^{-1}\ 5^6.\upsilon 5^8\ [h_{9/2}\, f_{7/2}]^2$ (Bands 5/6 in the experiment).

Figure 11 Same as for Figure 10 but for signature α=-1/2. Open symbols are used for two configurations of signature α=+1/2 in order to show that the calculations predict the observed signature degeneracy.

Figure 12 Same as for Fig. 10 but for experimental rotational bands in ^{133}Pm. The ($E-E_{RLD}$) curves for negative parity bands 1/2 and 7 are given in upper right corner scaled by 33% relative to main figure which means that the slopes of these curves are unchanged.

Figure 13 Experimental routhians for rotational bands in ^{133}Pm.

Figure 14 Total routhian surfaces at $\hbar\omega$ = 0.05 MeV for the (π,α)=(-,-1/2) proton configuration in (a) ^{137}Pm (b) ^{135}Pm and (c) ^{133}Pm. This configuration corresponds to the occupancy of a low-K $h_{11/2}$ orbital by the odd-proton, manifest as the decoupled yrast bands that are observed in these isotopes. Note the increasing, and less γ-soft, prolate deformation as the neutron number decreases.

TABLE 1
Gamma-Ray Transitions Assigned to ^{133}Pm

Band(s)	$E\gamma$ (keV)	Iγ	DCO Ratio[1)] A	DCO Ratio[1)] B	$J_i^\pi \rightarrow J_f^\pi$
1	252.8	140(3)	2.02(4)		$15/2^- \rightarrow 11/2^-$
	430.0	137(6)	1.99(5)		$19/2^- \rightarrow 15/2^-$
	571.4	104(5)	2.01(10)		$23/2^- \rightarrow 19/2^-$
	675.4	66(3)			$27/2^- \rightarrow 23/2^-$
	746.5	39(3)			$31/2^- \rightarrow 27/2^-$
	803.8	26(2)			$35/2^- \rightarrow 31/2^-$
	865.7(3)	21(2)			$39/2^- \rightarrow 35/2^-$
	934.3(5)	10(1)			$43/2^- \rightarrow 39/2^-$
	1005(1)	9(1)			$47/2^- \rightarrow 43/2^-$
	1078(1)	5(1)			$51/2^- \rightarrow 47/2^-$
	1154(2)	3.7(6)			$55/2^- \rightarrow 51/2^-$
2	262.9	25(1)	1.92(15)		$13/2^- \rightarrow 9/2^-$
	410.1	36(2)	2.08(17)		$17/2^- \rightarrow 13/2^-$
	513.9	41(3)	1.93(15)		$21/2^- \rightarrow 17/2^-$
	593.8	34(3)	2.09(20)		$25/2^- \rightarrow 21/2^-$
	670.5	25(3)			$29/2^- \rightarrow 25/2^-$
	749.8(2)	23(2)			$33/2^- \rightarrow 29/2^-$
	832.3(3)	16(2)			$37/2^- \rightarrow 33/2^-$
	915(1)	12(2)			$41/2^- \rightarrow 37/2^-$
	1003(1)	8(2)			$45/2^- \rightarrow 41/2^-$
1/2	281.1	23(1)	2.49(8)		$13/2^- \rightarrow 11/2^-$
	438.3	13(1)	2.36(10)		$17/2^- \rightarrow 15/2^-$
	522.2	9.5(6)	2.38(15)		$21/2^- \rightarrow 19/2^-$
	544.6	7.8(6)	1.7(2)		$25/2^- \rightarrow 23/2^-$
	539.7	5(1)	1.9(2)		$29/2^- \rightarrow 27/2^-$
3	214.7	5.8(6)			$7/2^+ \rightarrow 3/2^+$
	357.7	21.3(9)	1.99(9)		$11/2^+ \rightarrow 7/2^+$
	453.8	29(1)	1.98(10)		$15/2^+ \rightarrow 11/2^+$
	509.7	36.7(15)	1.92(15)		$19/2^+ \rightarrow 15/2^+$
	546.7	37.7(15)			$23/2^+ \rightarrow 19/2^+$
	592.9	31.6(20)			$27/2^+ \rightarrow 23/2^+$
	663.8(2)	22(1)			$31/2^+ \rightarrow 27/2^+$
	751.0(3)	19(2)			$35/2^+ \rightarrow 31/2^+$
	838(1)	15(2)			$39/2^+ \rightarrow 35/2^+$
	910(1)	10(2)			$43/2^+ \rightarrow 39/2^+$
	958(1)	9(3)			$47/2^+ \rightarrow 43/2^+$

TABLE 1 (Continued)
Gamma-Ray Transitions Assigned to ^{133}Pm

Band(s)	$E\gamma$ (keV)	Iγ	DCO Ratio[1)] A	DCO Ratio[1)] B	$J_i^\pi \rightarrow J_f^\pi$
4	297.9	17(8)	1.93(13)		$9/2^+ \rightarrow 5/2^+$
	420.8	27.2(12)	1.98(15)		$13/2^+ \rightarrow 9/2^+$
	492.5	29.2(15)	2.01(10)		$17/2^+ \rightarrow 13/2^+$
	535.9	29.4(15)			$21/2^+ \rightarrow 17/2^+$
	566.8	26.7(15)			$25/2^+ \rightarrow 21/2^+$
	594.5	22(2)			$29/2^+ \rightarrow 25/2^+$
	680.2(2)	13.5(7)			$33/2^+ \rightarrow 29/2^+$
	786.1(3)	12(1)			$37/2^+ \rightarrow 33/2^+$
	879(1)	8.9(1.8)			$41/2^+ \rightarrow 37/2^+$
	954(1)	5.7(1.5)			$45/2^+ \rightarrow 41/2^+$
3/4	84.6	~2			$5/2^+ \rightarrow 3/2^+$
	129.8	14.6(15)	1.45(5)	1.00(4)	$7/2^+ \rightarrow 5/2^+$
	167.5	13.0(6)	1.49(7)	1.07(4)	$9/2^+ \rightarrow 7/2^+$
	189.7	11.2(6)	1.43(11)	1.09(6)	$11/2^+ \rightarrow 9/2^+$
	230.7	8.9(5)	1.46(9)	1.06(8)	$13/2^+ \rightarrow 11/2^+$
	222.8	6.9(3)	1.35(9)	1.00(8)	$15/2^+ \rightarrow 13/2^+$
	269.4	6.8(4)	1.38(10)	0.93(10)	$17/2^+ \rightarrow 15/2^+$
	240.0	4.9(3)	1.38(10)	0.92(10)	$19/2^+ \rightarrow 17/2^+$
	295.6	5.6(3)	1.35(12)		$21/2^+ \rightarrow 19/2^+$
	250.8	3.6(2)			$23/2^+ \rightarrow 21/2^+$
	315.8(3)	4.7(4)			$25/2^+ \rightarrow 23/2^+$
	277.4(3)	2.3(2)			$27/2^+ \rightarrow 25/2^+$
	317.3(5)	2.4(3)			$29/2^+ \rightarrow 27/2^+$
5	338.4(3)	1.51(15)			$13/2^+ \rightarrow 9/2^+$
	434.5(2)	3.45(25)			$17/2^+ \rightarrow 13/2^+$
	526.8(2)	4.35(30)			$21/2^+ \rightarrow 17/2^+$
	615.5(2)	4.0(3)			$25/2^+ \rightarrow 21/2^+$
	704.3(4)	4.2(4)			$29/2^+ \rightarrow 25/2^+$
	787.7(2)	3.0(6)			$33/2^+ \rightarrow 29/2^+$
	866.7(3)	3.5(7)			$37/2^+ \rightarrow 33/2^+$
	946(1)	2.2(5)			$41/2^+ \rightarrow 37/2^+$
6	386.8(2)	2.27(20)			$15/2^+ \rightarrow 11/2^+$
	481.0(2)	3.84(25)			$19/2^+ \rightarrow 15/2^+$
	572.0(2)	4.0(3)			$23/2^+ \rightarrow 19/2^+$
	660.0(2)	3.5(4)			$27/2^+ \rightarrow 23/2^+$
	746.1(2)	3.7(6)			$31/2^+ \rightarrow 27/2^+$
	824.7(3)	3.0(6)			$35/2^+ \rightarrow 31/2^+$
	910(1)	2.0(5)			$39/2^+ \rightarrow 35/2^+$

TABLE 1 (Continued)
Gamma-Ray Transitions Assigned to ^{133}Pm

Band(s)	$E\gamma$ (keV)	Iγ	DCO Ratio[1)] A	DCO Ratio[1)] B	$J_i^\pi \rightarrow J_f^\pi$
5/6	156.5	5.4(3)		1.21(12)	$11/2^+ \rightarrow 9/2^+$
	181.2	6.0(3)		1.28(12)	$13/2^+ \rightarrow 11/2^+$
	205.3	6.8(3)		1.21(12)	$15/2^+ \rightarrow 13/2^+$
	228.8	5.3(3)		1.25(12)	$17/2^+ \rightarrow 15/2^+$
	251.8	4.5(3)			$19/2^+ \rightarrow 17/2^+$
	274.6	4.0(3)		1.23(15)	$21/2^+ \rightarrow 19/2^+$
	297.1	3.0(4)			$23/2^+ \rightarrow 21/2^+$
	318.4	2.2(5)			$25/2^+ \rightarrow 23/2^+$
	341.4	1.9(4)			$27/2^+ \rightarrow 25/2^+$
	362.6(2)	1.4(3)			$29/2^+ \rightarrow 27/2^+$
	383.7(4)	1.6(4)			$31/2^+ \rightarrow 29/2^+$
	404(1)	1.0(4)			$33/2^+ \rightarrow 31/2^+$
From Band 5	271.6(10)	0.9(1)			$9/2^+ \rightarrow 9/2^+$
	439.1(2)	3.7(3)	1.27(25)		$9/2^+ \rightarrow 7/2^+$
	281.6(2)	3.3(3)	1.30.(35)		$9/2^+ \rightarrow (7/2)^+$
	287.4(2)	2.1(1)	1.22(15)		$(7/2)^+ \rightarrow 5/2^+$
	372.6(7)	1.2(6)			$(7/2)^+ \rightarrow 3/2^+$
3/1	643(1)	4.3(4)	1.9(2)		$15/2^+ \rightarrow 15/2^-$
	723(1)	5.3(4)	1.7(2)		$19/2^+ \rightarrow 19/2^-$
	698(1)	3.7(4)	1.8(2)		$23/2^+ \rightarrow (23/2)^-$
7	411.0(3)	5.6(5)			$(19/2)^- \rightarrow (15/2)^-$
	531.4	14.9(7)			$(23/2)^- \rightarrow (19/2)^-$
	630.3	19.2(9)			$(27/2)^- \rightarrow (23/2)^-$
	725.9(3)	16.2(16)			$(31/2)^- \rightarrow (27/2)^-$
	796(1)	8(3)			$(35/2)^- \rightarrow (31/2)^-$
	862(1)	~4			$(39/2)^- \rightarrow (35/2)^-$
7/1	433.9	5.4(7)	2.05(15)		$(15/2)^- \rightarrow 15/2^-$
	415.0	5.9(6)	1.95(25)		$(19/2)^- \rightarrow 19/2^-$
	374.9	3.8(3)	2.10(15)		$(23/2)^- \rightarrow 23/2^-$
	329.9	2.1(3)			$(27/2)^- \rightarrow 27/2^-$
	309.5	2.2(3)			$(31/2)^- \rightarrow 31/2^-$
7/2	405.1(4)	3.0(3)			$(15/2)^- \rightarrow 13/2^-$
	406.6(3)	5.4(4)	1.9(2)		$(19/2)^- \rightarrow 17/2^-$
	424.1(3)	4.3(3)	1.8(3)		$(23/2)^- \rightarrow 21/2^-$
	461.1(2)	3.8(4)			$(27/2)^- \rightarrow 25/2^-$
	516.6(3)	1.6(3)			$(31/2)^- \rightarrow 29/2^-$

1) DCO Ratios are Iγγ (±37°, ±37°)/Iγγ (±79°, ±79°).
- Values in column A refer to averages over adjacent gating transitions known to be ΔJ=2, *E*2.
- Values in column B refer to averages over adjacent ΔJ=1 mixed M1/*E*2 transitions and are meaningful only for transitions between signature-partner bands, cf text.

TABLE 2
Summary of E2/M1 Mixing Ratios, δ, M1 and E2 Reduced Matrix Elements

	Initial Spin I	γ-ray Transition (keV)	B(M1)/B(E2) x [1 + δ^2]	δ A mixed-E2	δ B mixed-mixed	B(E2; J→J-1)/ B(E2; J→J-2)
Band 3/4	7/2	130	0.36(4)	0.188(25)	0.150(16)	$0.68^{0.16}_{0.12}$
	9/2	168	0.263(14)	0.212(35)	0.178(16)	$0.42^{0.08}_{0.08}$
	11/2	190	0.31(2)	0.18(6)	0.195(24)	$0.46^{0.11}_{0.11}$
	13/2	231	0.244(14)	0.19(5)	0.175(30)	$0.20^{0.07}_{0.07}$
	15/2	223	0.281(16)	0.13(5)	0.15(3)	$0.18^{0.07}_{0.07}$
	17/2	269	0.243(16)	0.15(6)	0.12(4)	$0.07^{0.06}_{0.05}$
	19/2	240	0.23(2)	0.15(6)	0.12(4)	$0.08^{0.06}_{0.05}$
	21/2	296	0.226(15)	0.13(6)		
	23/2	251	0.209(13)			
	25/2	316	0.23(2)			
	27/2	277	0.18(2)			
	29/2	318	0.18(2)			
Band 5/6	11/2	157			0.23(3)	
	13/2	181	2.05(25)		0.25(3)	$5.3^{1.3}_{1.1}$
	15/2	205	2.1(2)		0.23(3)	3.5(9)
	17/2	229	1.31(12)		0.24(3)	2.0(5)
	19/2	252	1.31(12)			
	21/2	274	1.26(13)		0.23(5)	1.2(5)
	23/2	297	1.18(18)			
	25/2	318	1.06(25)			
	27/2	341	1.2(3)			

TABLE 2
Summary of E2/M1 Mixing Ratios, δ, M1 and E2 Reduced Matrix Elements (Continued)

	Initial Spin I	γ-ray Transition (keV)	B(M1)/B(E2) x $[1 + \delta^2]$	δ A	δ B	B(E2; J→J-1)/ B(E2; J→J-2)
Band 2/1	13/2	281	0.036(2)	~1		
	17/2	438	0.035(3)	~1		
	21/2	522	0.033(3)	~1		
	25/2	545	0.07(1)			
	29/2	540	0.120(15)			

TABLE 3: Summary of Measured Q_o - Values and Derived Deformation Parameters

Band	Measured Q_o eb	Deformation Parameter β_2	Deformation Parameter ε
1	5.2(5)	0.29(3)[a)]	0.25(3)
3/4	5.4(6)	0.29(3)	0.255(30)
5/6	7.4(10)	0.40(5)	0.33(4)

a) Previous result: $\beta_2 = 0.333(14)$ (ref. 23)

Table 4: The calculated deformations of superdeformed configurations at two different spin values.

Configuration	ε_2	ε_4	γ	ε_2	ε_4	γ
	π = +, α = + 1/2					
	I = 10.5$\hbar$			I = 46.5$\hbar$		
$\pi 5^4\ \upsilon 5^6[h_{9/2}\ f_{7/2}]^2 6^1$	0.353	-0.010	1.6°	0.292	0.015	7.5°
$\pi 5^4 6^1\ \upsilon 5^6[h_{9/2}\ f_{7/2}]^2 6^2$	0.375	-0.023	1.4°	0.357	0.0	4.8°
$\pi 5^6[g_{9/2}]^{-1}\ \upsilon 5^8[h_{9/2}\ f7/2]^2$	0.359	0.036	0.6°	0.317	0.014	1.0°
	π = +, α = - 1/2					
	I = 11.5$\hbar$			I = 47.5$\hbar$		
$\pi 5^5\ \upsilon 5^7[h_{9/2}\ f_{7/2}]^2 6^1$	0.353	0.008	1.3°	0.316	0.026	4.6°
$\pi 5^4\ \upsilon 5^6[h_{9/2}\ f_{7/2}]^2 6^2$	0.358	-0.010	0.1°	0.328	0.017	6.0°
$\pi 5^6[g_{9/2}]$-1 $\upsilon 5^8[h_{9/2}\ f_{7/2}]^2$	0.361	0.036	0.2°	0.311	0.013	0.9°

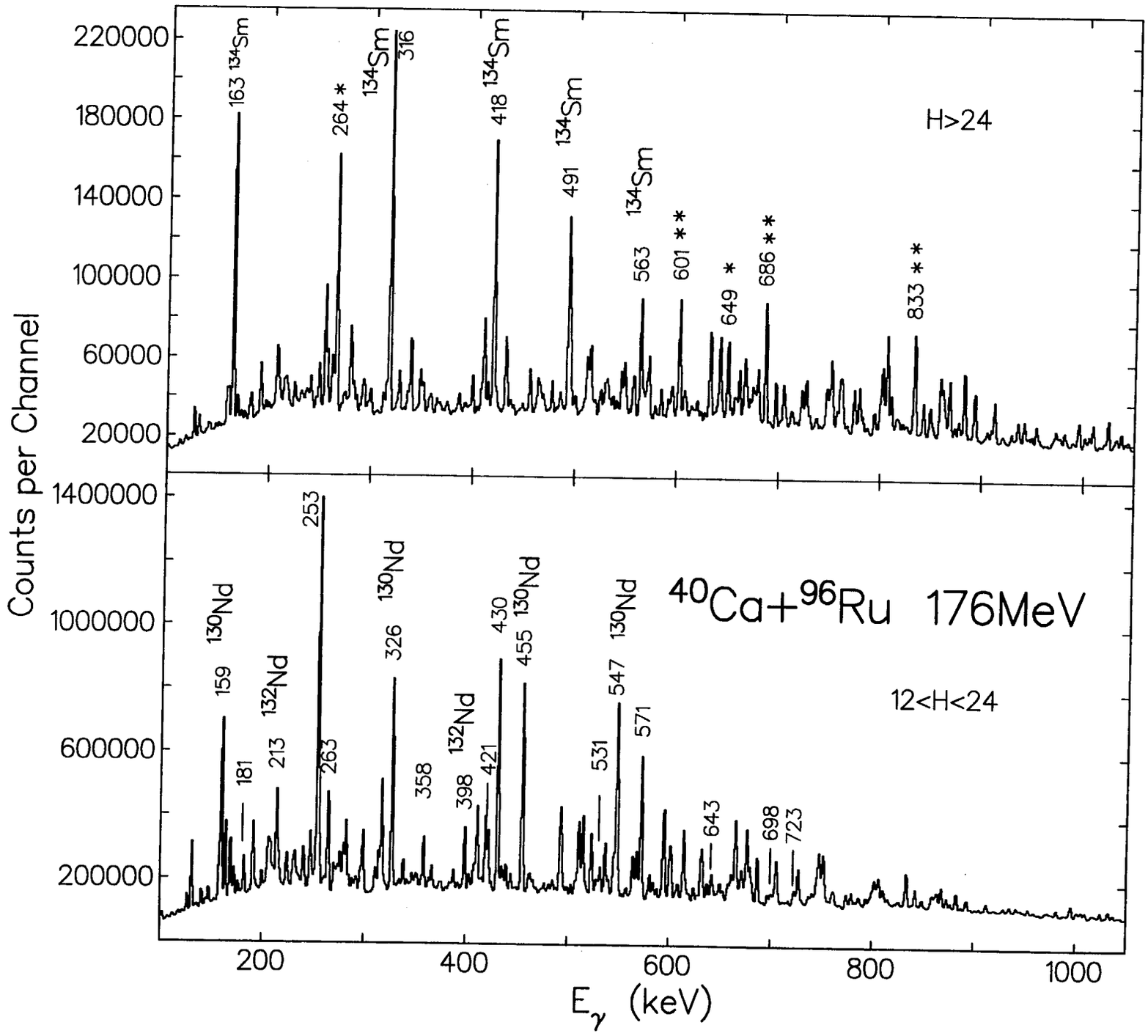
Counts per Channel
220000
180000
140000
100000
60000
20000
1400000
1000000
600000
200000
200
400
600
800
1000
E_γ (keV)
H>24
163 ^{134}Sm
264 *
^{134}Sm
316
418 ^{134}Sm
491 ^{134}Sm
563 ^{134}Sm
601 **
649 *
686 **
833 **
^{40}Ca+^{96}Ru 176MeV
12<H<24
159 ^{130}Nd
181
213 ^{132}Nd
253
263
326 ^{130}Nd
358
398 ^{132}Nd
421
430
455 ^{130}Nd
531
547 ^{130}Nd
571
643
698
723

Fig 1

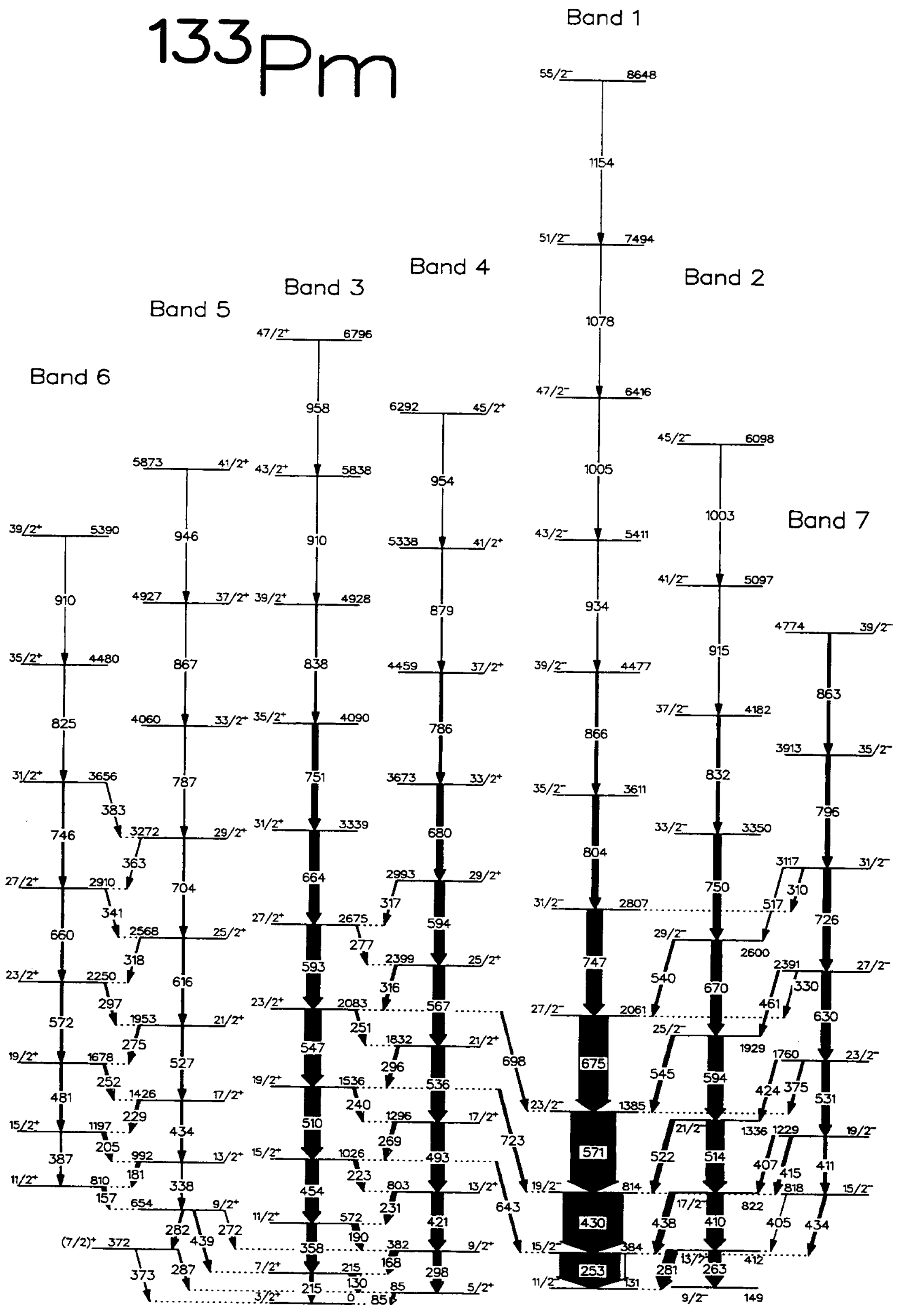
133Pm
Band 1
55/2− 8648
1154
51/2− 7494
1078
47/2− 6416
1005
43/2− 5411
934
39/2− 4477
866
35/2− 3611
804
31/2− 2807
747
27/2− 2061
675
23/2− 1385
571
19/2− 814
430
15/2− 384
253
11/2− 131
Band 2
45/2− 6098
1003
41/2− 5097
915
37/2− 4182
832
33/2− 3350
750
29/2− 2600
670
25/2− 1929
594
21/2− 1336
514
17/2− 822
410
13/2− 412
263
9/2− 149
540
545
522
438
281
517
461
424
407
405
Band 7
4774 39/2−
863
3913 35/2−
796
3117 31/2−
726
2391 27/2−
630
1760 23/2−
531
1229 19/2−
411
818 15/2−
434
310
330
375
415
Band 4
6292 45/2+
954
5338 41/2+
879
4459 37/2+
786
3673 33/2+
680
2993 29/2+
594
2399 25/2+
567
1832 21/2+
536
1296 17/2+
493
803 13/2+
421
382 9/2+
298
85 5/2+
698
723
643
Band 3
47/2+ 6796
958
43/2+ 5838
910
39/2+ 4928
838
35/2+ 4090
751
31/2+ 3339
664
27/2+ 2675
593
23/2+ 2083
547
19/2+ 1536
510
15/2+ 1026
454
11/2+ 572
358
7/2+ 215
215
3/2+ 0
317
277
316
251
296
240
269
223
231
190
168
130
85
Band 5
5873 41/2+
946
4927 37/2+
867
4060 33/2+
787
3272 29/2+
704
2568 25/2+
616
1953 21/2+
527
1426 17/2+
434
992 13/2+
338
654 9/2+
282
439
272
287
363
318
275
229
181
Band 6
39/2+ 5390
910
35/2+ 4480
825
31/2+ 3656
746
27/2+ 2910
660
23/2+ 2250
572
19/2+ 1678
481
15/2+ 1197
387
11/2+ 810
383
341
297
252
205
157
(7/2)+ 372
373

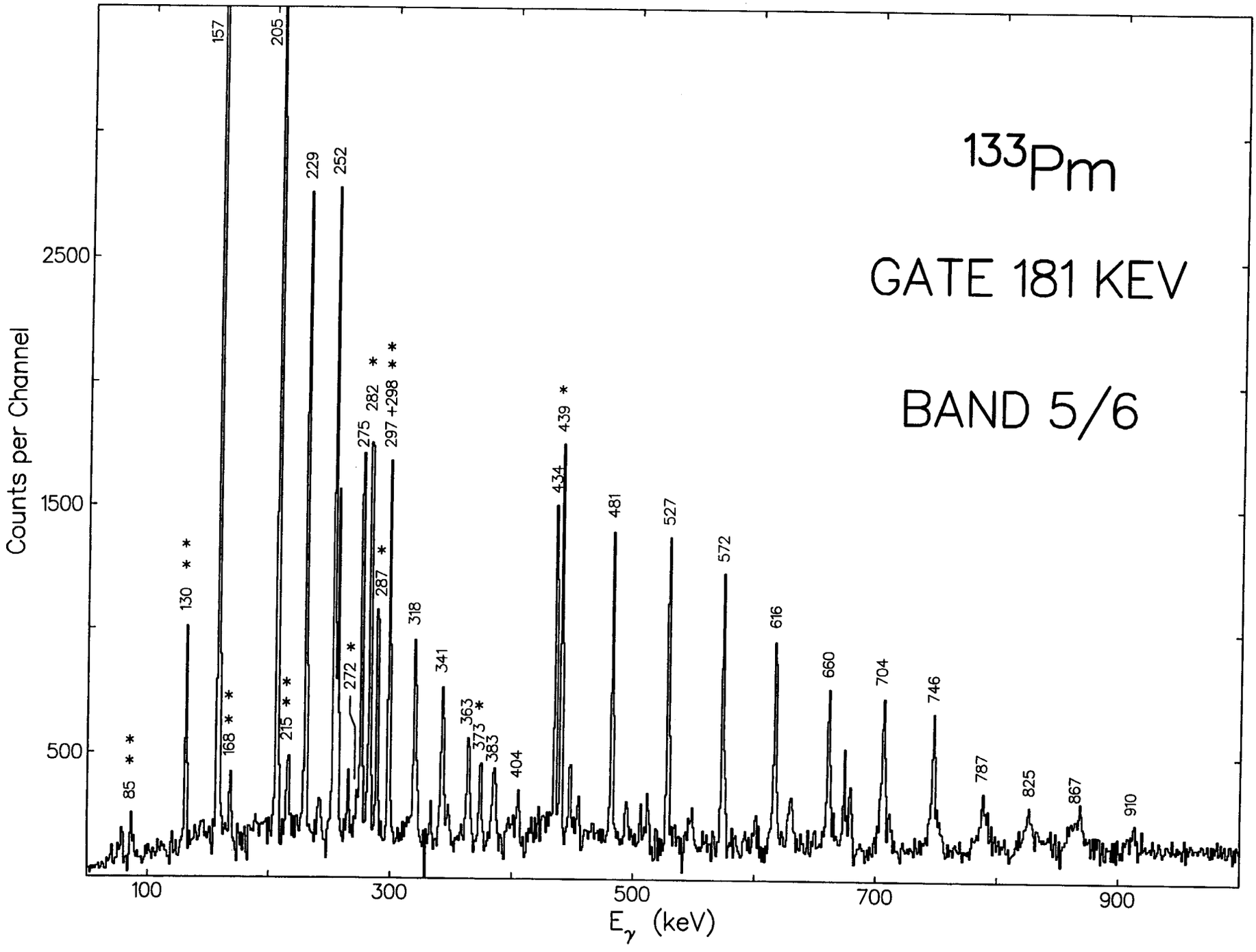
^{133}Pm
GATE 181 KEV
BAND 5/6
Counts per Channel
2500
1500
500
100
300
500
700
900
E_γ (keV)
85 * *
130 * *
157
168 * *
205
215 * *
229
252
272 *
275
282 *
297 +298 * *
287 *
318
341
363
373 *
383
404
434
439 *
481
527
572
616
660
704
746
787
825
867
910

Fig 3

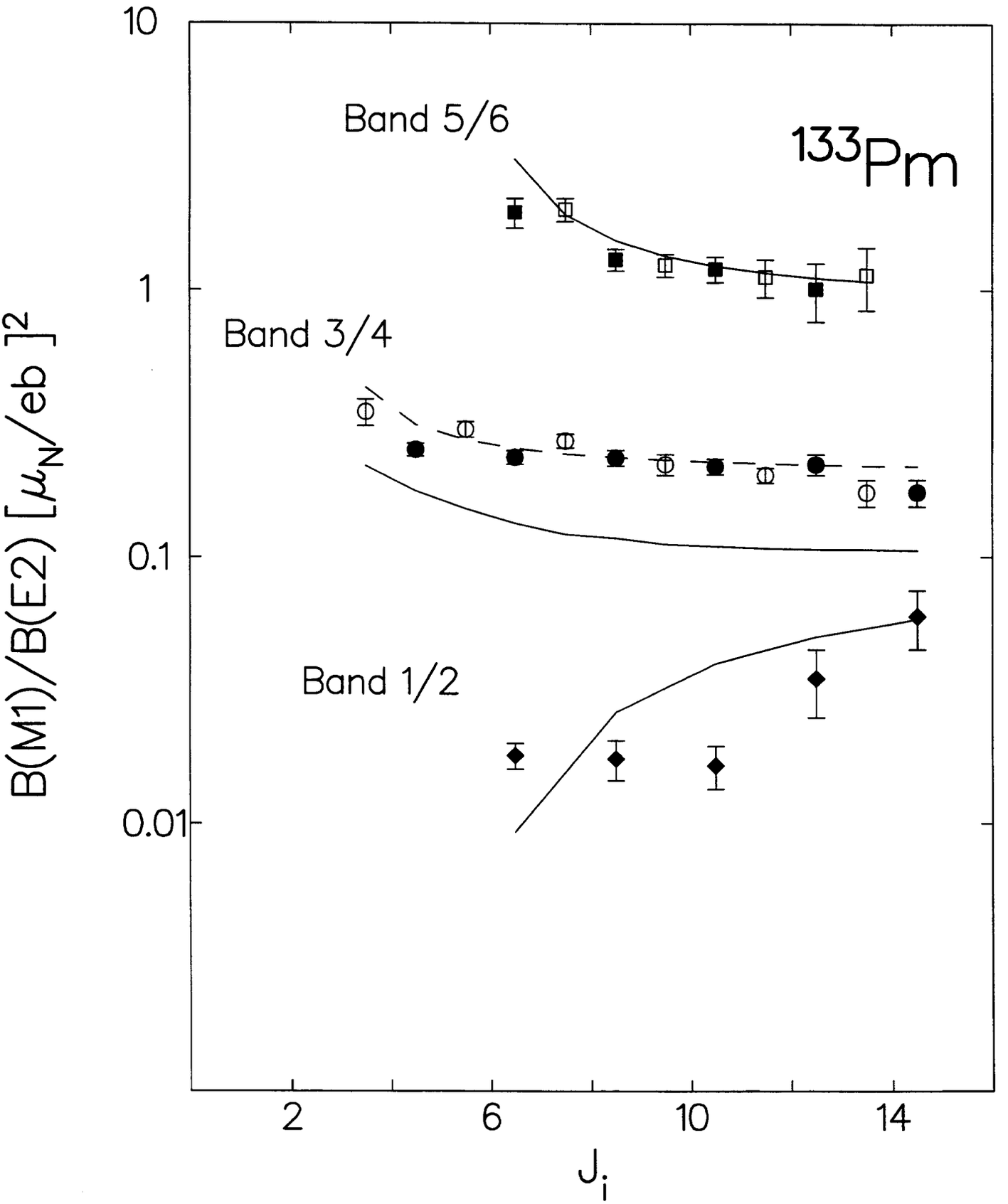
10
1
0.1
0.01
B(M1)/B(E2) [μ_N/eb]^2
Band 5/6
^{133}Pm
Band 3/4
Band 1/2
2
6
10
14
J_i

Fig 4

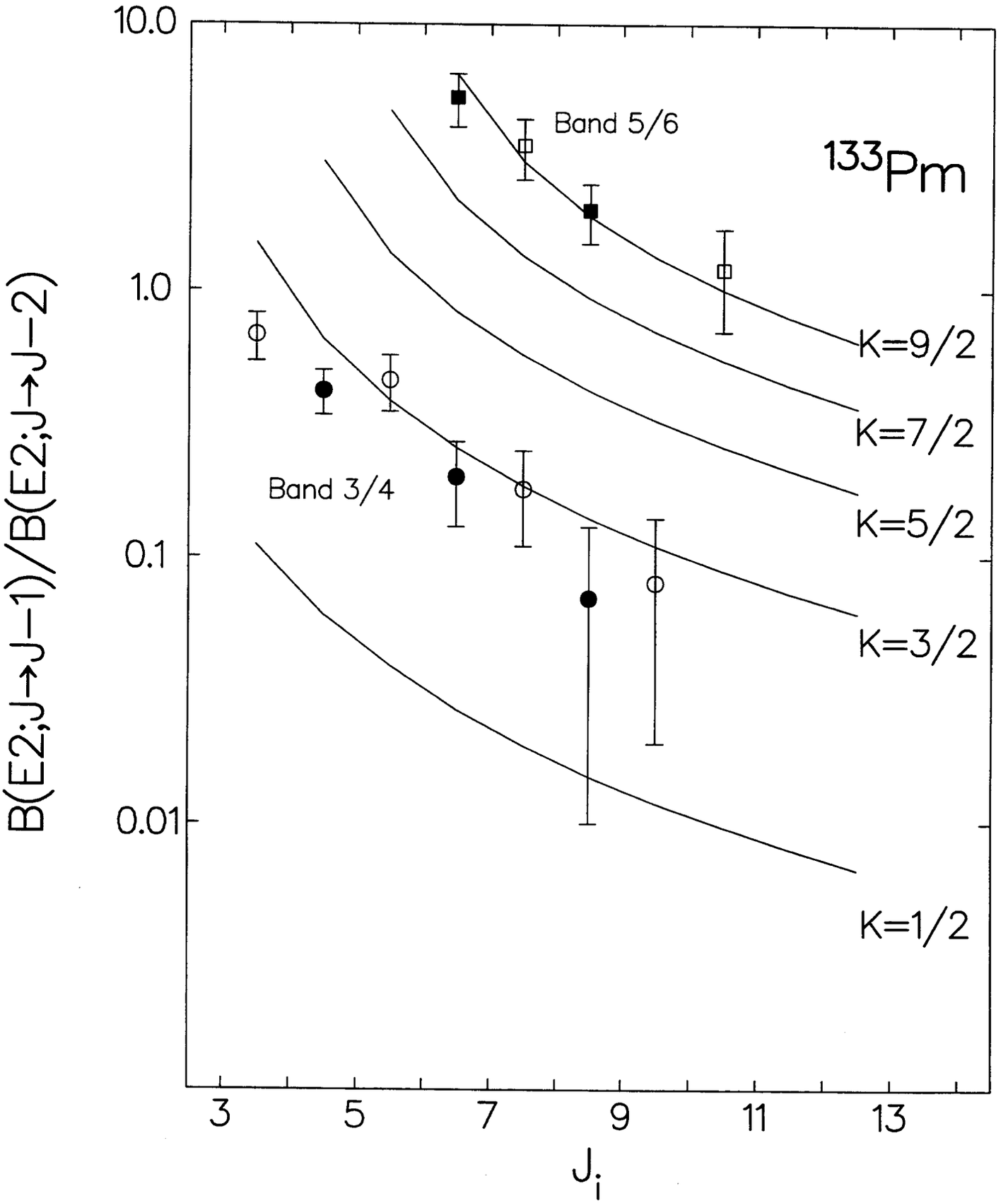
10.0
1.0
0.1
0.01
B(E2;J→J−1)/B(E2;J→J−2)
3
5
7
9
11
13
J_i
Band 5/6
Band 3/4
^{133}Pm
K=9/2
K=7/2
K=5/2
K=3/2
K=1/2

Fig 5

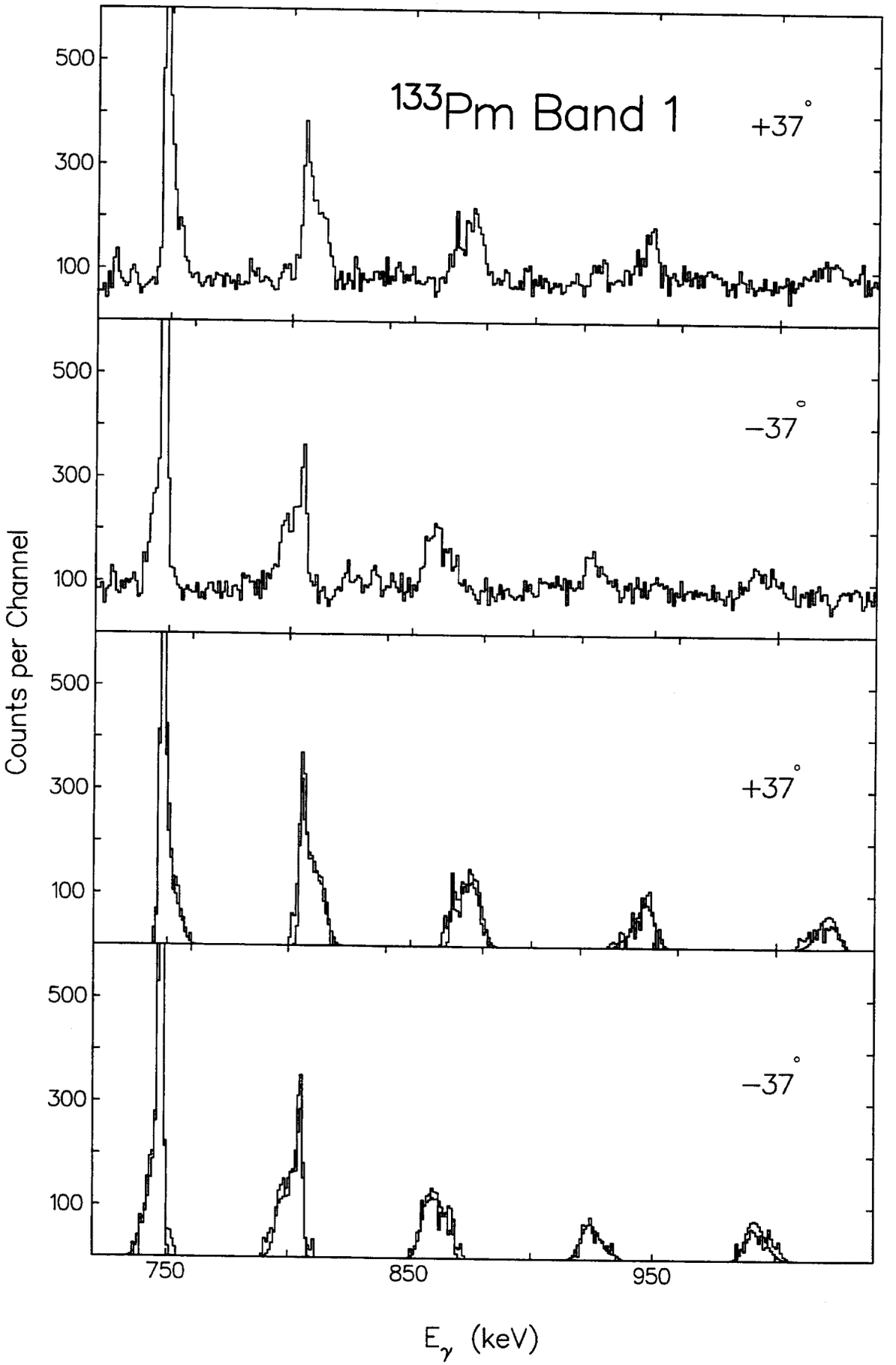
133Pm Band 1
+37°
−37°
+37°
−37°
500
300
100
Counts per Channel
750
850
950
Eγ (keV)

Fig 6

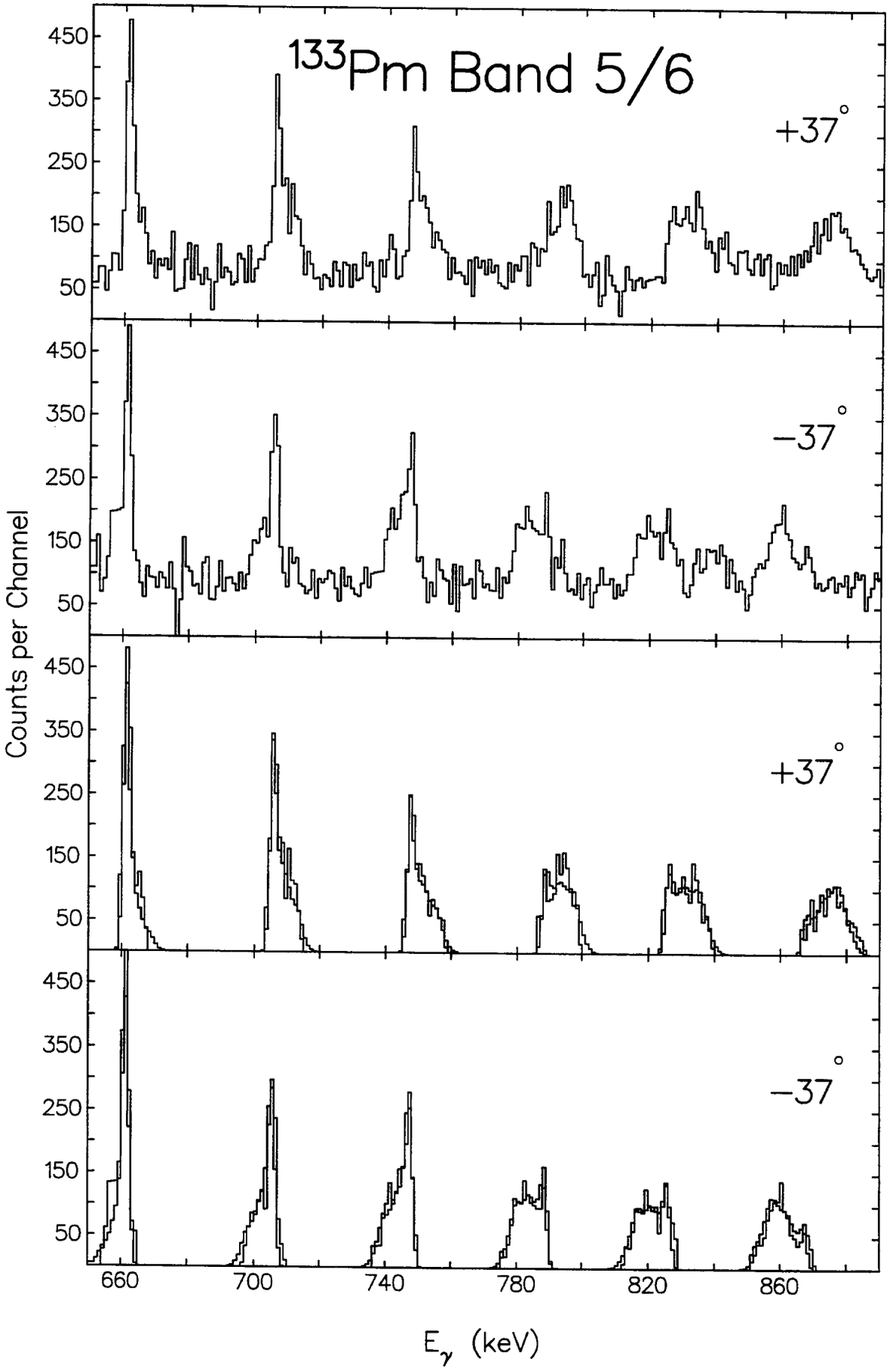
133Pm Band 5/6
+37°
−37°
+37°
−37°
Counts per Channel
450
350
250
150
50
660
700
740
780
820
860
Eγ (keV)

Gq 7

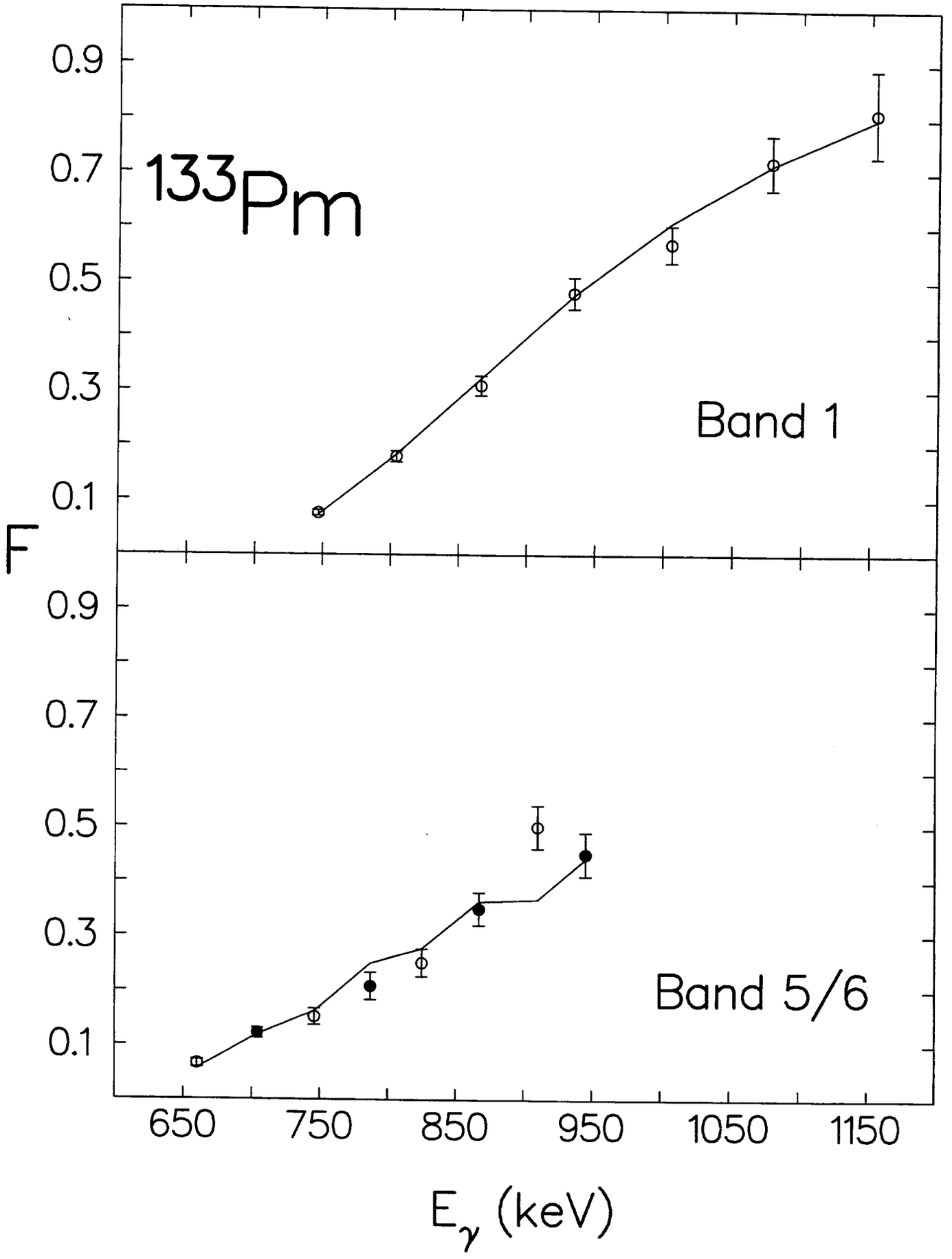
^{133}Pm
Band 1
Band 5/6
F
0.9
0.7
0.5
0.3
0.1
650
750
850
950
1050
1150
E_γ (keV)

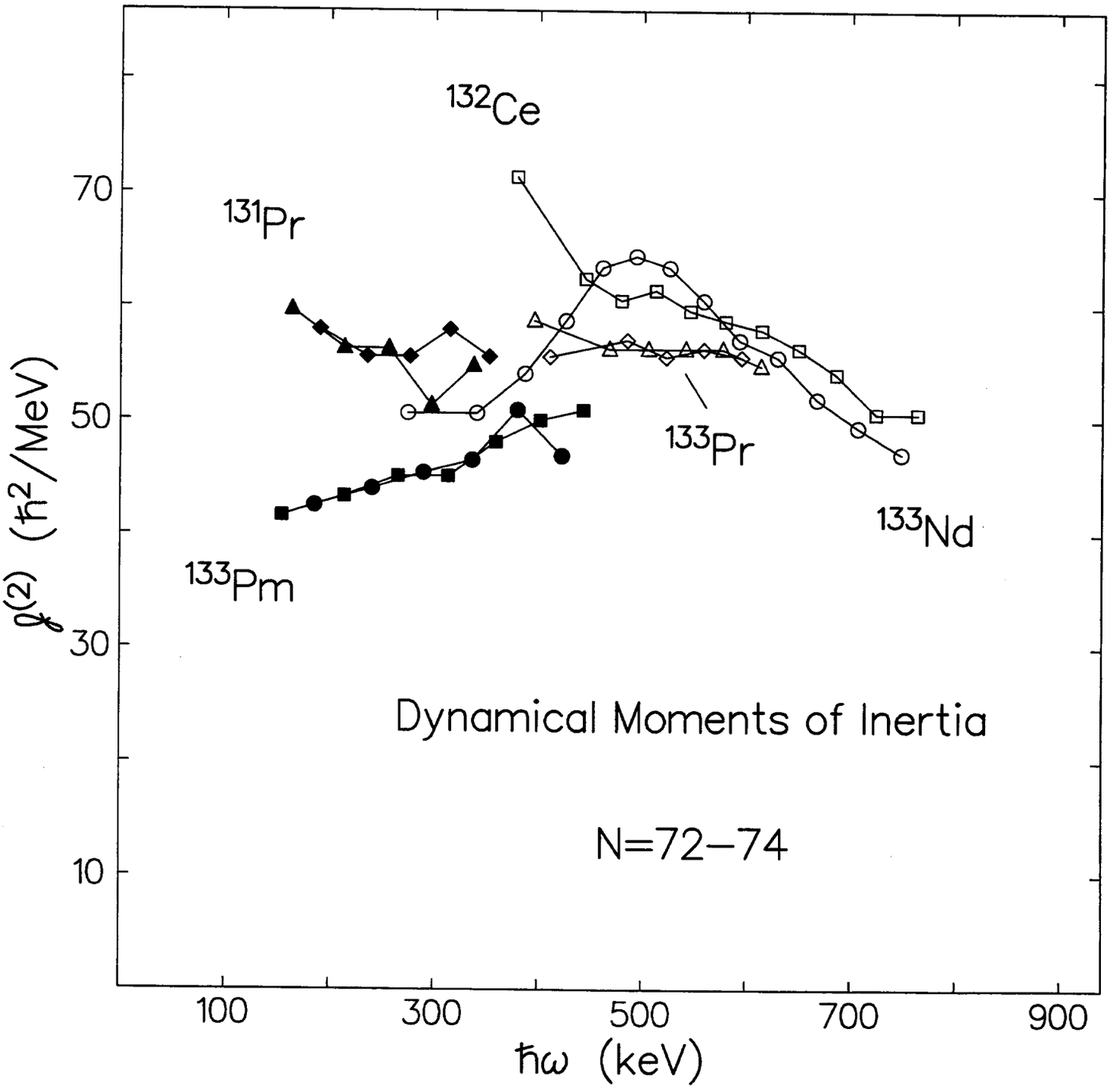
^{132}Ce
^{131}Pr
^{133}Pr
^{133}Nd
^{133}Pm
Dynamical Moments of Inertia
N=72–74
$\mathcal{J}^{(2)}$ ($\hbar^2$/MeV)
70
50
30
10
100
300
500
700
900
$\hbar\omega$ (keV)

Fig 9(a)

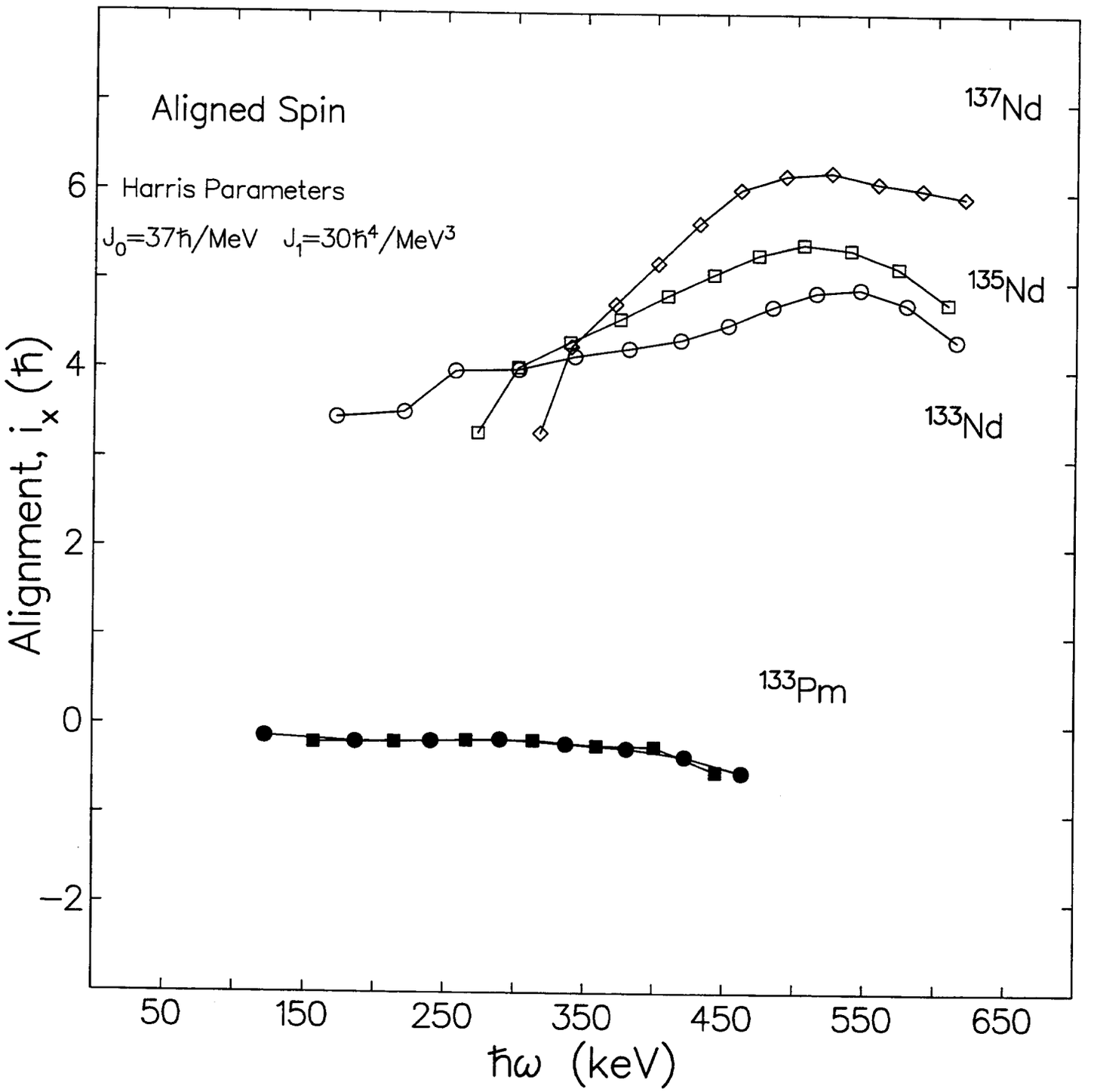
Aligned Spin
Harris Parameters
J_0=37ħ/MeV J_1=30ħ⁴/MeV³
^{137}Nd
^{135}Nd
^{133}Nd
^{133}Pm
Alignment, i_x (ħ)
ħω (keV)
6
4
2
0
−2
50
150
250
350
450
550
650

Fig 9(b)

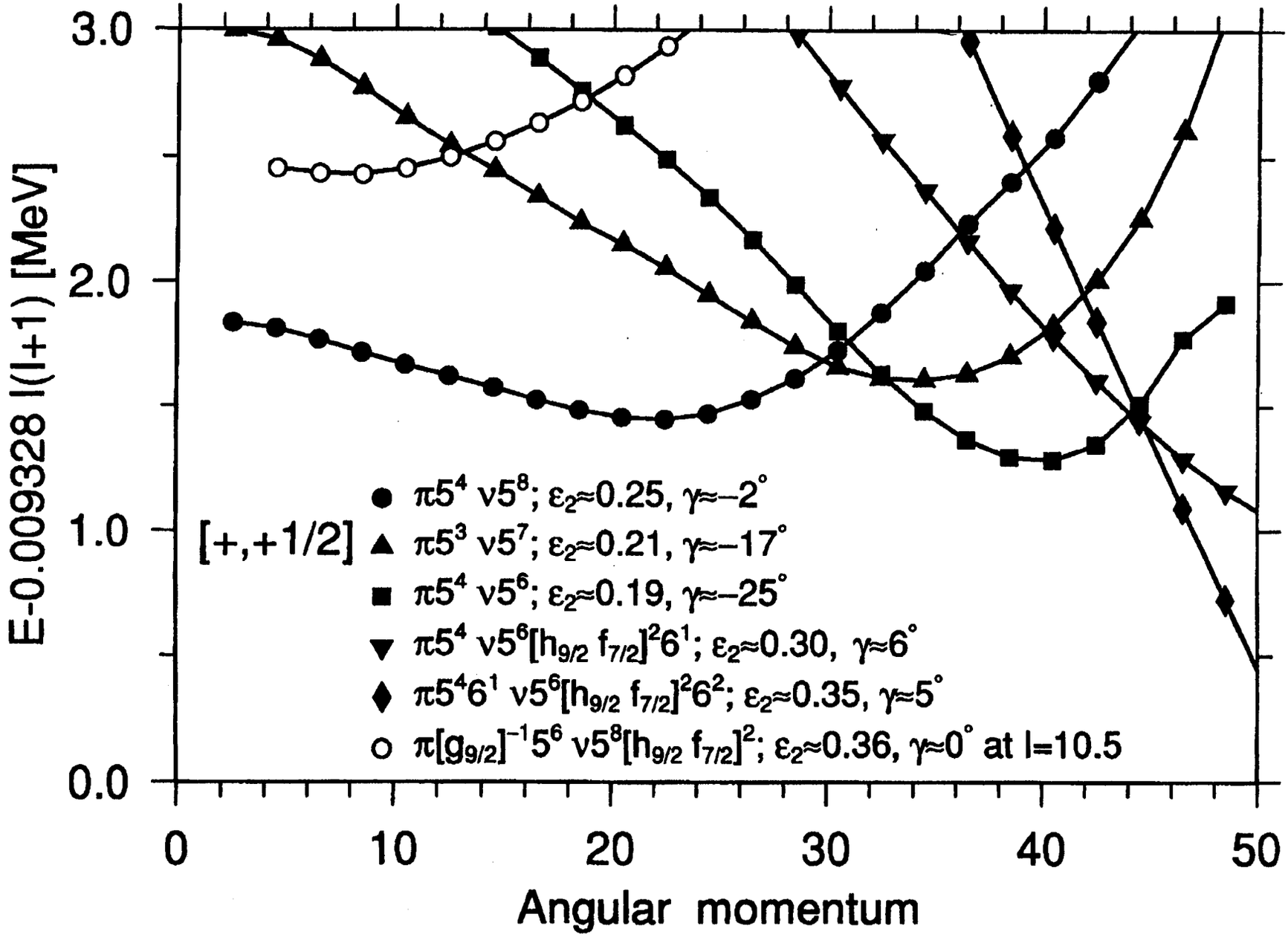
3.0
2.0
1.0
0.0
E-0.009328 I(I+1) [MeV]
0
10
20
30
40
50
Angular momentum
[+,+1/2]
π5^4 ν5^8; ε2≈0.25, γ≈−2°
π5^3 ν5^7; ε2≈0.21, γ≈−17°
π5^4 ν5^6; ε2≈0.19, γ≈−25°
π5^4 ν5^6[h9/2 f7/2]^2 6^1; ε2≈0.30, γ≈6°
π5^4 6^1 ν5^6[h9/2 f7/2]^2 6^2; ε2≈0.35, γ≈5°
π[g9/2]^-1 5^6 ν5^8[h9/2 f7/2]^2; ε2≈0.36, γ≈0° at I=10.5

Fig 10

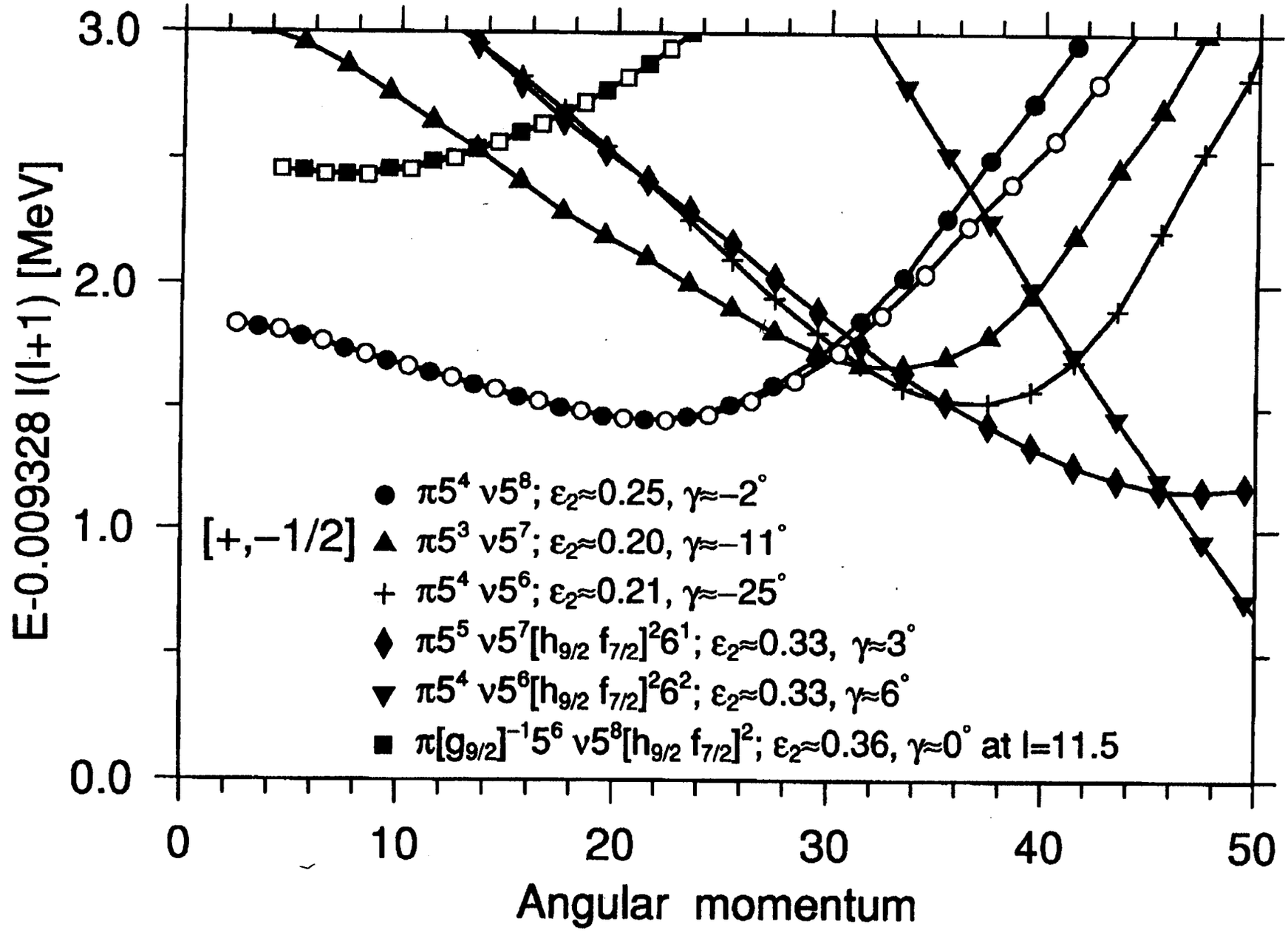
3.0
2.0
1.0
0.0
E-0.009328 I(I+1) [MeV]
0
10
20
30
40
50
Angular momentum
[+,−1/2]
π5⁴ ν5⁸; ε₂≈0.25, γ≈−2°
π5³ ν5⁷; ε₂≈0.20, γ≈−11°
π5⁴ ν5⁶; ε₂≈0.21, γ≈−25°
π5⁵ ν5⁷[h9/2 f7/2]²6¹; ε₂≈0.33, γ≈3°
π5⁴ ν5⁶[h9/2 f7/2]²6²; ε₂≈0.33, γ≈6°
π[g9/2]⁻¹5⁶ ν5⁸[h9/2 f7/2]²; ε₂≈0.36, γ≈0° at I=11.5

Fig 11

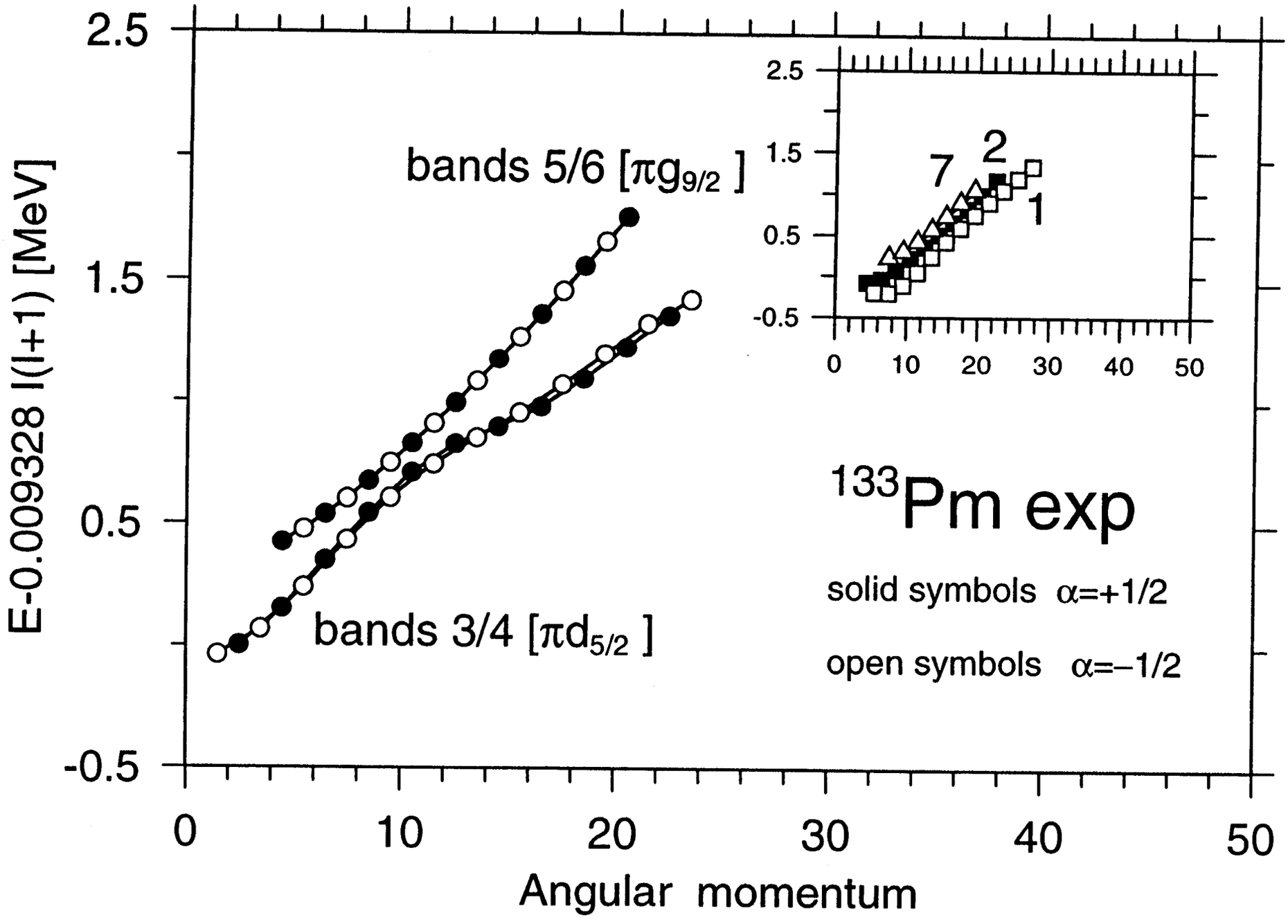
2.5
1.5
0.5
-0.5
E-0.009328 I(I+1) [MeV]
0
10
20
30
40
50
Angular momentum
bands 5/6 [πg9/2]
bands 3/4 [πd5/2]
133Pm exp
solid symbols α=+1/2
open symbols α=−1/2
7
2
1

Gg 12

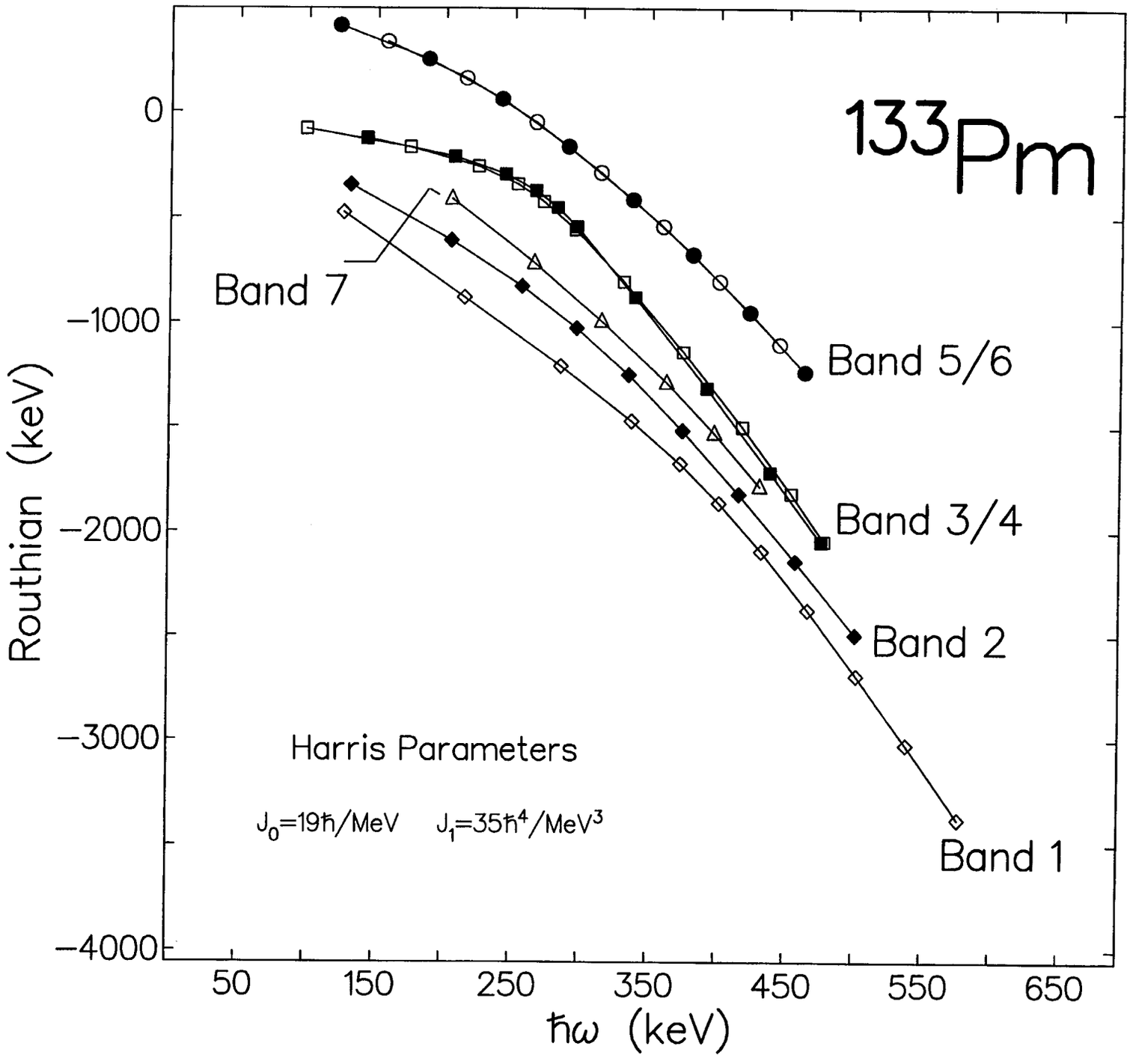
133Pm
Band 7
Band 5/6
Band 3/4
Band 2
Band 1
Harris Parameters
J0=19ħ/MeV J1=35ħ4/MeV3
Routhian (keV)
ħω (keV)
0
−1000
−2000
−3000
−4000
50
150
250
350
450
550
650

Gq 13

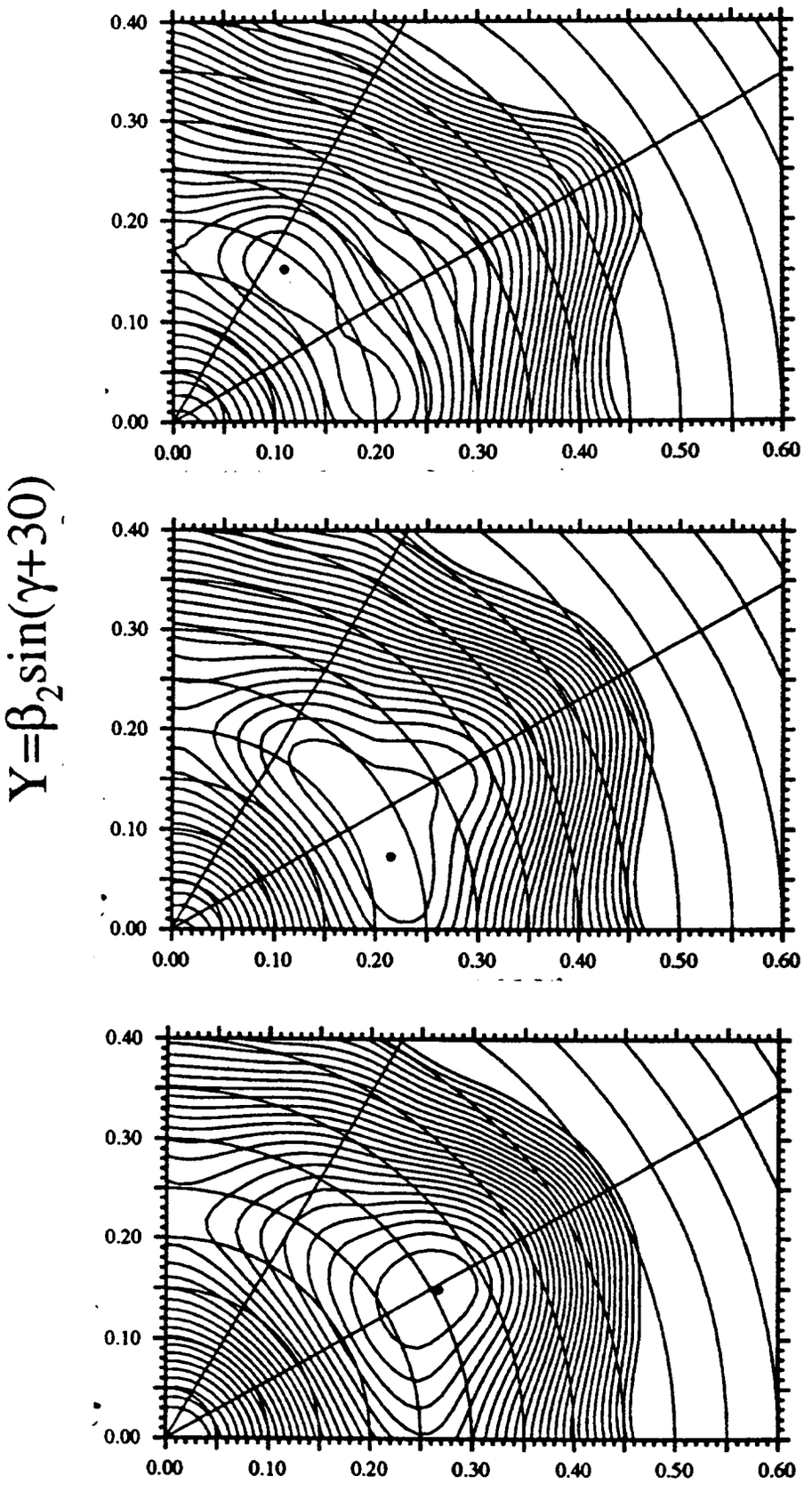
0.40
0.30
0.20
0.10
0.00
0.00
0.10
0.20
0.30
0.40
0.50
0.60
Y=β2sin(γ+30)
X=β2cos(γ+30)

Fig 14